ANNALS OF GEOPHYSICS, 69, 2026, doi:10.4401/ag-9650
OPEN ACCESS

Integrated Analysis of Stress Transfer, Vp/Vs Variations and Seismicity Clustering during the 2025 Santorini-Amorgos Seismic Swarm

Kyriaki Pavlou[*,1], Eirini Sardeli[1], Andreas Karakonstantis[1,2], Filippos Vallianatos[1,3]

(1) Section of Geophysics-Geothermics, Department of Geology and Geoenvironment, National and Kapodistrian University of Athens, 15784 Athens, Greece.
(2) University of Patras, Patra, Greece.
(3) Institute of Physics of Earth's Interior and Geohazards, UNESCO Chair on Solid Earth Physics and Geohazards Risk Reduction, Hellenic Mediterranean University Research & Innovation Center, 73133 Chania, Greece

Article history: received Month DD, YYYY; accepted November 16, 2026

Abstract

The 2025 Santorini-Amorgos seismic swarm represents one of the most significant recent episodes of seismic activity within the South Aegean Volcanic Arc. This study investigates its spatiotemporal evolution by integrating Coulomb Failure Stress (ΔCFS) modelling, Vp/Vs ratio analysis using the Wadati method, and fractal correlation dimension (D_c) analysis of earthquake hypocenters.

A high-resolution earthquake catalogue comprising 13,707 relocated events, was analyzed for the January-March 2025 Santorini-Amorgos seismic sequence. From this dataset, events within the selected study period and magnitude range were considered, as well as the focal mechanism solutions for earthquakes of moment magnitude $M_w \geq 4.7$ were used to calculate Coulomb Failure Stress changes (ΔCFS). Positive ΔCFS values were calculated at the hypocenters of several selected subsequent earthquakes, indicating that the modelled static stress changes were favorable to fault activation at these locations. These results are consistent with a possible contribution of static stress transfer to the evolution of the seismic sequence, although its relative contribution to the overall swarm development cannot be established from the present analysis.

Temporal variations in the Vp/Vs ratio were estimated from 1,125 earthquakes with $M_L \geq 3.0$, grouped into successive datasets. Vp/Vs estimates ranged from ~1.70 to ~1.78 and showed temporal variability during the most active phase of the swarm. These variations likely may be interpreted as possible indicators of transient changes in pore-fluid conditions within the activated fault-fracture system, although formal uncertainties are not available for the individual set-specific estimates and fluid migration cannot be uniquely established from Vp/Vs variations alone.

The spatial fractal correlation dimension D_c, calculated using a moving-window approach, showed pronounced temporal variability. D_c exceeded 2 during the early stage of the sequence and subsequently decreased to a minimum of 0.84 (95% CI: 0.80-0.88) on 6-7 February 2025. This decrease indicates a transition towards a lower-dimensional spatial organization of earthquake hypocenters over the analyzed spatial scales.

The combined evolution of ΔCFS, Vp/Vs, and D_c is consistent with the possible involvement of static stress redistribution, transient fluid-related processes, and changes in the spatial organization of seismicity during the 2025 Santorini-Amorgos swarm. These results provide a complementary

interpretation of the possible processes involved in the evolution of the Santorini-Amorgos seismic swarm, without establishing a direct causal relationship among the examined parameters.

Keywords: Santorini-Amorgos seismic sequence; Coulomb stress changes; Vp/Vs ratio; Fractal correlation dimension D_c; Fluid migration

1. Introduction

The Santorini Volcanic Complex (SVC) is one of the most active volcanic and tectonic centers of the South Aegean Volcanic Arc, where seismicity is driven by both tectonic deformation and magmatic or hydrothermal processes. Earthquakes in the region are typically of small to moderate magnitude and frequently occur as seismic swarms, reflecting dynamic processes at depth (Papadimitriou et al., 2015).

The Santorini Volcanic Complex lies within the back-arc domain of the Hellenic subduction zone, where the African Plate subducts beneath the Eurasian Plate (McKenzie, 1978). Most tectonic faults exhibit a NE-SW orientation consistent with the dominant structural trend of the Santorini-Kolumbo volcano-tectonic line (Heiken and McCoy, 1984). This zone links the Santorini caldera with the active submarine Kolumbo volcano (Druitt et al., 1999; Nomikou et al., 2013; Karakonstantis and Vallianatos, 2024; Mrlina and Sakkas, 2026) and has been repeatedly associated with historical eruptions and recent seismic swarms (Papadopoulos, 2026), highlighting the interplay between tectonic deformation and magmatic activity.

Low-level microseismicity was recorded within the caldera in mid-2024, followed by increased activity in September. A previous notable swarm occurred in 2011-2012 (Kaviris et al., 2015; Papadimitriou et al., 2015; Vallianatos et al., 2013). In early 2025, the region experienced intense seismic activity lasting several weeks (Zaccagnino et al., 2025; Polat and Altin, 2026; Sarlis et al., 2026; Soubestre et al., 2026; Wilding et al., 2026; Yolsal-Çevikbilen et al., 2026). Since 27 January 2025, 8,688 seismic events of magnitude $M_L \geq 1.5$ were recorded offshore between Santorini and Amorgos, beginning within the caldera and migrating northeastward. The largest event reached M_L 5.0 on 10 February 2025. The spatial distribution of the sequence is illustrated in Fig. 1 showing that seismicity was mainly concentrated offshore between Santorini and Amorgos and followed a predominantly NE-SW trending zone.

Earthquake swarms in volcanic-tectonic environments may be driven by aseismic slip, fluid intrusion, pore-pressure diffusion, or stress transfer from preceding events (Chouet, 2003; Hainzl et al., 2006; Chen et al., 2012; Michas et al., 2022). They typically involve numerous small to moderate earthquakes (M 1.0-5.0) and rarely produce large events (Srijayanthi et al., 2022).

The central question of this study is whether the migration and temporal evolution of the 2025 Santorini-Amorgos swarm can be explained by static Coulomb stress redistribution, or whether additional transient processes – such as pore-fluid pressure changes and reorganization of the activated fault-fracture network – are required.

To address this, we integrate three complementary approaches:

(i) modelling Coulomb Failure Stress changes (ΔCFS) for the strongest events to assess whether subsequent earthquakes occurred in positively stressed regions;
(ii) analyzing temporal variations of the Vp/Vs ratio using the Wadati method to infer possible changes in pore-fluid conditions; and
(iii) computing the spatial fractal correlation dimension D_c to characterize temporal changes in the spatial organization of earthquake hypocenters over the analyzed spatial scales.

By combining stress-transfer modelling, seismic velocity-ratio variations, and fractal characterization of hypocentral distributions, this study provides an integrated physical interpretation of the 2025 Santorini-Amorgos swarm and explores the possible contributions of the stress redistribution, transient fluid-related processes, and changes in the spatial organization of seismicity during its evolution.

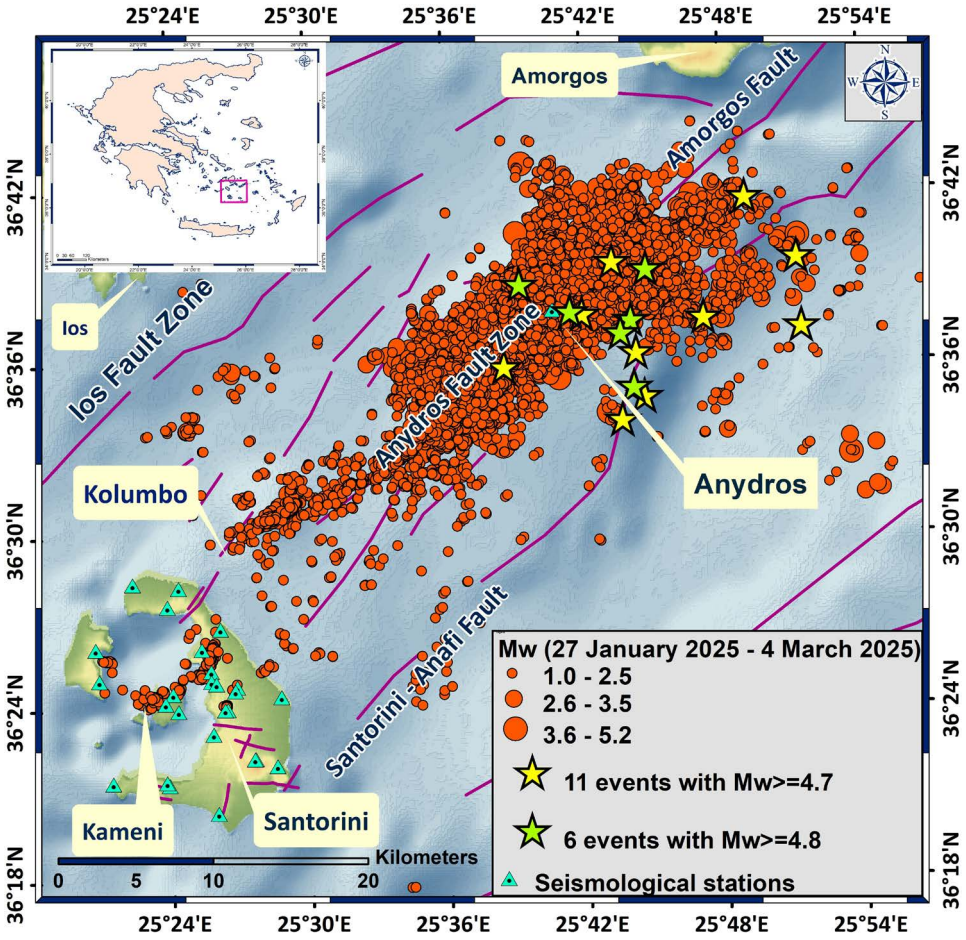

Figure 1. Spatial distribution of seismicity in the Santorini-Amorgos area from 27 January to 4 March 2025. Orange circles indicate earthquake epicenters, with symbol size corresponding to magnitude. Stars mark the epicenters of the 17 earthquakes with $M_w \geq 4.7$ used for Coulomb stress modelling (Table 1): lime-green stars denote the six events selected for detailed ΔCFS analysis (Table 2), and yellow stars denote the remaining 11 events. Turquoise triangles indicate seismological stations, and purple lines represent faults (Ganas, 2025).

2. Seismotectonic regime

Santorini Volcanic Complex is one of the largest Quaternary volcanic centers in the Aegean region. It is situated in the central part of the South Aegean Volcanic Arc and is considered the most active center in the region. The island of Santorini has undergone at least nine eruptions in the past 600 years, specifically in the years 1457, 1508, 1573, 1650, 1707, 1866, 1925, 1939, and 1950 (Fytikas et al., 1990; Papadopoulos, 2026; Papazachos and Papazachou, 2003). Seismic swarms associated with periods of volcanic unrest have also been documented, particularly during the 2011-2012 unrest episode (Vallianatos et al., 2013; Papadimitriou et al., 2015; Kaviris et al., 2015).

Most tectonic faults in SVC strike SW-NE (Heiken and McCoy, 1984). Key volcanic centres – including the Christiana Islands and the submarine Kolumbo volcano, located ~7 km northeast of Santorini – are aligned along two major structural lineaments: the Kameni Line and the Kolumbo Line. These fault systems traverse the Santorini caldera from northeast to southwest and form the primary volcano-tectonic corridor linking Santorini with Kolumbo. The island is composed predominantly of volcanic rocks, except for its southeastern sector, where Mesozoic-Cenozoic metamorphic limestones and schists form the pre-volcanic basement (Nicholls, 1971; Druitt et al., 1989).

The oldest preserved lavas on Santorini occur on the Akrotiri Peninsula and date to approximately 650 ka (Druitt et al., 1999). The most prominent event was the Minoan eruption, extensively studied by Heiken and McCoy (1984, 1990). The long-term volcanic evolution has produced a diverse assemblage of lithologies, including basalts, andesites, dacites, rhyodacites, rhyolites, tephra deposits, and ignimbrites (Druitt et al., 1999; Heiken and McCoy, 1984).

Figure 2 illustrates the spatial distribution of seismicity in the Santorini region using data compiled from three sources. Instrumental seismicity for period 1 January 1900 to 31 December 2009 was obtained from the catalogue of Makropoulos et al. (2012), whereas seismicity from 1 January 2010 to 31 December 2024 was provided by the Seismological Laboratory of the National and Kapodistrian University of Athens (http://dggsl.geol.uoa.gr). The historical earthquakes of 1650 (M 6.3) and 1866 (M 6.1) were obtained from Papazachos and Papazachou (2003). The left panel shows earthquakes with M > 4.0 during 1900 to 2022, together with these two historical events. The right panel shows seismicity during 2023-2024 within the Santorini-Amorgos zone, where dense clusters of small to moderate earthquakes align with major NE-SW trending faults.

Shallow seismicity extends from northeastern Santorini toward southwestern Amorgos, concentrated mainly in the Anydros and Amorgos basins and along the Santorini-Amorgos Ridge.

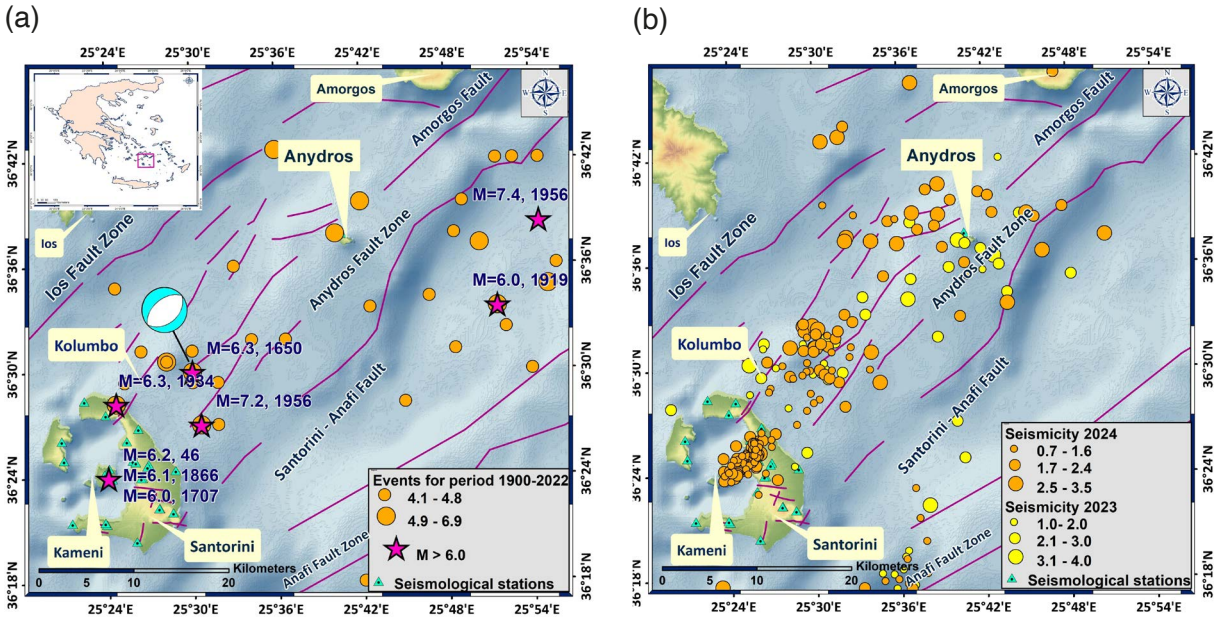

Figure 2. Seismicity map of notable earthquakes preceding the 2025 Santorini-Amorgos swarm. The circles and stars (stronger events) represent seismic events (a) from 1900-2022 and (b) from 2023-2024, illustrating long-term and recent seismic activity in the region. Major tectonic faults are shown in purple lines (Ganas, 2025).

3. Seismic Data

The dataset used in this study is the high-resolution dataset developed by Fountoulakis and Evangelidis (2025) for the 2024-2025 Santorini-Amorgos seismic sequence, comprising a total of 13,707 accurately located events. From this catalogue, we selected events occurring between 27 January and 4 March 2025 with local magnitude $M_L \geq 1.5$ for our analysis. The catalogue was generated through a fully automated, multi-step processing workflow that combines deep-learning-based phase picking, event association, absolute and relative hypocentral relocation, and magnitude estimation. The catalogue is publicly available and serves as the foundation for the seismic sequence analysis presented here (https://zenodo.org/record/15074928).

Within the study area, 30 events occurred during the last days of January 2025, and 6,917 earthquakes of local magnitude $M_L \geq 1.5$ were recorded in the first 15 days of February (Fig. 3). The day with the highest activity was February 6, 2025, with 679 events recorded. Additionally, the depth distribution of seismicity ranges from 0 to 30 km, while magnitudes range from 1.5 to 5.0.

For the analysis of Coulomb stress changes during the 2025 Santorini-Amorgos seismic swarm, we used Centroid Moment Tensor (CMT) focal mechanism solutions provided by the National Observatory of Athens for the period 1 January to 18 February 2025 (https://bbnet.gein.noa.gr/HL/seismicity/mts). Seismic events with moment magnitude $M_w \geq 4.7$ were selected for ΔCFS modelling, as these earthquakes are expected to dominate the static stress redistribution within the study area (Table 1).

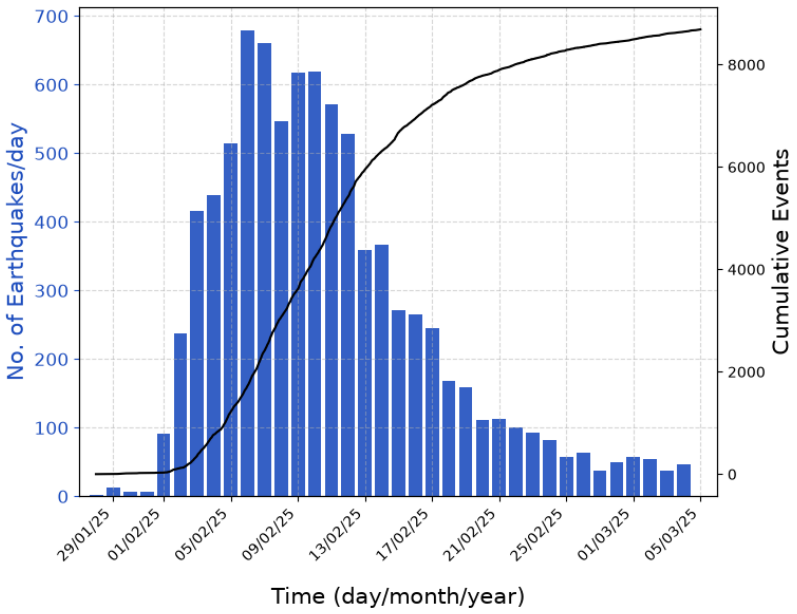

Figure 3. Daily number of seismic events recorded between 27 January and 4 March 2025. The black line shows the cumulative number of earthquakes in the Santorini region.

To investigate the spatiotemporal variations of the Vp/Vs velocity ratio, two complementary seismological datasets were employed. Earthquake data covering the period January 2011 to June 2025 were obtained from the Seismological Laboratory of the National and Kapodistrian University of Athens (NKUA). For the intense seismic sequence between 25 January and 4 March 2025, we used the high-resolution earthquake catalogue of Fountoulakis and Evangelidis (2025), which provides improved hypocentral locations for the Santorini-Amorgos swarm. Within this interval, 1,140 earthquakes with local magnitude $M_L \geq 3.0$ were selected. Of these, 15 spatially isolated events, located at relatively large distances from the main seismicity concentration, were excluded to improve the spatial coherence of the analyzed dataset. The remaining 1,125 earthquakes were arranged chronologically into 75 consecutive, non-overlapping sets of 15 events each, based on origin time. For each set, P- and S-wave arrival times were used to estimate the Vp/Vs ratio using the Wadati method (Wadati and Oki, 1933).

4. Coulomb Stress Changes

4.1 Methodology

Numerous studies on major earthquakes have demonstrated a strong correlation between positive Coulomb stress changes and the spatial evolution of seismic events (King et al., 1994; Vallianatos and Pavlou, 2021). Coulomb Failure Stress changes (ΔCFS) generated by large earthquakes may either accelerate or delay subsequent seismic activity, thereby influencing both the temporal and spatial distribution of earthquakes (Stein, 1999; Kilb et al., 2002). A positive ΔCFS transferred to a receiver fault brings it closer to failure, whereas a negative ΔCFS indicates a reduction in failure potential.

The Coulomb Failure Stress change (ΔCFS) on a receiver fault is calculated from the changes in shear and normal stresses resolved on the fault plane and is expressed as (Scholz, 2019; Toda et al., 2011):

$$\Delta CFS = \Delta\tau - \mu\Delta\sigma \tag{1}$$

where $\Delta\tau$ represents the change in static shear stress, $\Delta\sigma$ is the change in normal stress, and μ is the friction coefficient of the fault.

The Coulomb stress changes (ΔCFS) were calculated using the Coulomb 3.3 software (Toda et al., 2011), which operates under the assumption of an elastic half-space. Each earthquake was modelled assuming uniform slip on a rectangular rupture plane. The ΔCFS calculations were performed using a friction coefficient of $\mu = 0.4$, a commonly adopted value in Coulomb stress transfer modeling, as indicated in the Coulomb 3.3 User Guide (Toda et al., 2011). This value was adopted as a modelling assumption rather than as a direct measurement of the frictional properties of the Santorini-Amorgos fault system. Additionally, the empirical relations established by Wells and Coppersmith (1994) were used to determine the width and length of the subsurface seismic faults associated with each modeled earthquake (Lin and Stein, 2004; Toda et al., 2005). In this way, Coulomb stress changes were calculated for the 17 strongest earthquakes of magnitude $M_w \geq 4.7$ that occurred during the seismic swarm from early January to late February 2025.

The Coulomb stress calculations represent deterministic model estimates for the prescribed source and receiver parameters; therefore, formal statistical uncertainties are not directly obtained. To evaluate the sensitivity of the calculated ΔCFS values to the assumed friction coefficient, ΔCFS at the selected receiver locations was recalculated using $\mu = 0.2$ and $\mu = 0.6$, in addition to the reference value $\mu = 0.4$. The sensitivity calculation was performed using the resolved shear and normal stress components according to Eq. (1). Other sources of model uncertainty include focal-mechanism parameters, source depth, rupture geometry and dimensions, and the assumption of uniform slip; these uncertainties were not independently propagated in the present analysis.

Table 1. Focal mechanisms of $M_w \geq 4.7$ events used for Coulomb modelling. All focal mechanisms obtained from the National Observatory of Athens (NOA), (https://bbnet.gein.noa.gr/HL/seismicity/mts).

No	Date	Time	Latitude	Longitude	Depth	M_w	Strike	Dip	Rake
1	03/02/2025	09:29	36.5854	25.7364	13.7	4.8	41	52	−117
2	03/02/2025	12:17	36.6389	25.7478	10.5	4.8	50	55	−86
3	03/02/2025	20:19	36.6289	25.6975	13.9	4.8	14	78	−161
4	04/02/2025	02:46	36.6197	25.7066	14.3	4.7	44	51	−97
5	04/02/2025	13:04	36.6167	25.727	5.0	5.0	44	48	−98
6	05/02/2025	19:09	36.6582	25.7213	11.2	5.0	45	48	−80
7	07/02/2025	07:16	36.5664	25.7278	7.0	4.7	19	56	−127
8	08/02/2025	09:00	36.5799	25.7439	5.0	4.7	35	55	−118
9	09/02/2025	19:05	36.6454	25.6544	11.2	5.1	26	62	−133
10	10/02/2025	11:23	36.6602	25.8546	10.0	4.7	15	79	−172
11	10/02/2025	20:16	36.6538	25.7456	5.0	5.2	207	66	−154
12	10/02/2025	22:37	36.6255	25.787	10.0	4.9	50	45	−92
13	11/02/2025	05:58	36.6952	25.8178	5.0	4.7	192	79	179
14	12/02/2025	08:29	36.4071	25.9418	5.0	4.8	221	85	−164
15	12/02/2025	09:15	36.5977	25.6425	8.8	4.7	247	37	−57
16	17/02/2025	07:49	36.599	25.7047	5.1	4.8	233	43	−82
17	18/02/2025	04:46	36.6199	25.8577	5.0	4.9	39	46	−110

4.2 Results

Within SVC, small-magnitude events began to be recorded in the Santorini caldera and around the Kolumbo volcano in September 2024, migrated offshore between Santorini-Amorgos, with seismic activity intensifying after 26 January 2025. On 3 February 2025, three significant earthquakes occurred – two M_w 4.8 events at 09:29 and 12:17 (UTC), followed by another M_w 4.8 event at 20:19 (UTC). During the subsequent days and until 18 February 2025, an additional 14 earthquakes with $M_w \geq 4.7$ were recorded in the Santorini-Amorgos region.

To investigate the progression of the seismic sequence, coseismic static Coulomb stress changes were computed for the 17 earthquakes listed in Table 1. For detailed analysis and cumulative ΔCFS calculations at the centroids of the earthquake sets, six source earthquakes were selected based on magnitude, occurrence time and epicentral location (Table 2). We considered events with $M_w \geq 4.8$ occurring up to and including the largest earthquake of the sequence on 10 February 2025 at 20:16 UTC, and preferentially selected sources located centrally within the main seismicity concentration. This spatial selection was qualitative, based on visual inspection of the epicentral distribution, rather than on a predefined distance threshold. The M_w 5.0 earthquake of 5 February 2025 at 19:09 UTC met the magnitude and temporal criteria but was not included because its epicenter was judged less central to the seismicity concentration targeted by this analysis. The aim was to examine whether the cumulative static stress contribution from the selected sources could have favored subsequent seismicity. These calculations represent the contribution of the six selected sources and don't include the contributions of the remaining modelled earthquakes.

For the three M_w 4.8 earthquakes of 3 February 2025, the spatial distribution of ΔCFS shows positive stress changes toward the NE and SW, and negative changes toward the NW and SE (Fig. 4). Earthquakes with $M_L \geq 3.0$ recorded up to 18 February (shown as pink circles) exhibit a spatial distribution aligned with the strike of the activated fault system. The hypocenters are superimposed on the modeled stress fields to illustrate the spatial relationship between seismicity and static stress redistribution. However, this qualitative comparison does not establish a preferential occurrence of subsequent earthquakes within positive ΔCFS regions or demonstrate a causal relationship between static stress transfer and earthquake occurrence.

Table 2. Six selected source earthquakes used for detailed ΔCFS analysis and cumulative stress calculations at the centroids of the earthquake sets.

No	Date Time	Latitude	Longitude	Depth	M_w	Strike	Dip	Rake
1	03/02/2025 09:29	36.5854	25.7364	13.7	4.8	41	52	−117
2	03/02/2025 12:17	36.6389	25.7478	10.5	4.8	50	55	−86
3	03/02/2025 20:19	36.6289	25.6975	13.9	4.8	14	78	−161
4	04/02/2025 13:04	36.6167	25.727	5.0	5.0	44	48	−98
5	09/02/2025 19:05	36.6454	25.6544	11.2	5.1	26	62	−133
6	10/02/2025 20:16	36.6538	25.7456	5.0	5.2	207	66	−154

Figure 5 illustrates the spatial distribution of static Coulomb stress changes associated with the M_w 5.0 earthquake on 4 February 2025, which occurred at 13:04 (UTC). The ΔCFS pattern shows positive stress changes toward the NE and SW and negative changes toward the NW and SE, consistent with the distribution expected for normal-faulting events in an elastic half-space.

The earthquake hypocenters are plotted on the calculated ΔCFS distribution to illustrate the spatial relationship between seismicity and the stress changes induced by the M_w 5.0 event. The modeled positive ΔCFS lobes are generally aligned with the NE-SW orientation of the activated fault system, which also corresponds to the predominant direction of the seismicity. This spatial correspondence is presented as a qualitative observation and does not, by itself, establish a preferential occurrence of earthquakes within positive stress regions.

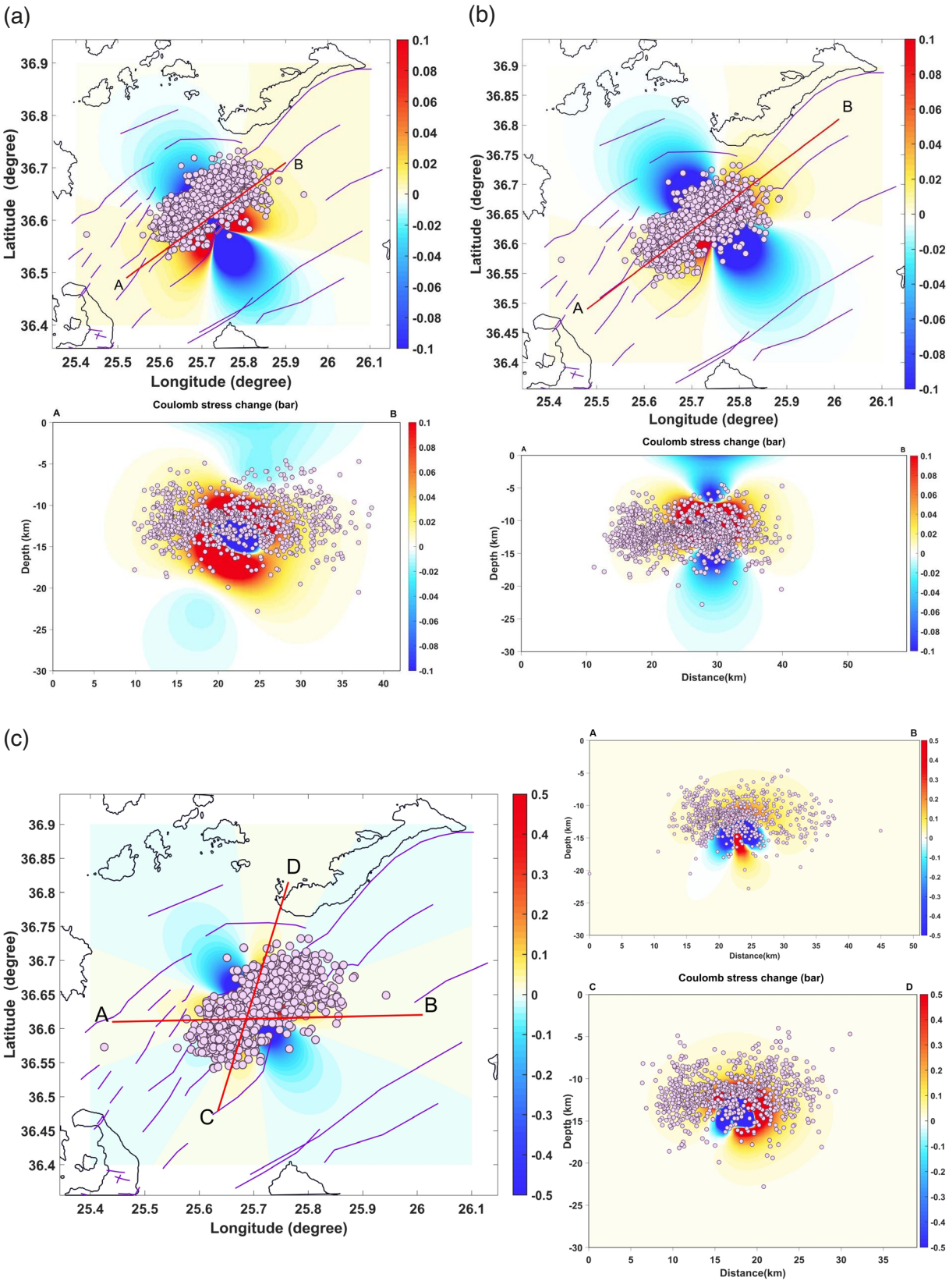

Figure 4. Coseismic Coulomb stress change distributions resulting from the earthquakes that occurred on February 3, 2025: (a) M_w 4.8 earthquake at 9:29, (b) the M_w 4.8 earthquake on the same day at 12:17, and (c) M_w 4.8 earthquake at 20:19 with centroid depths of 13.7 km, 10.5 km and 13.9 km, respectively. Pink circles denote the hypocenters of swarm events recorded up to 18 February 2025. Cross-sections A-B and C-D illustrate the depth-dependent distribution of the ΔCFS associated with these earthquakes.

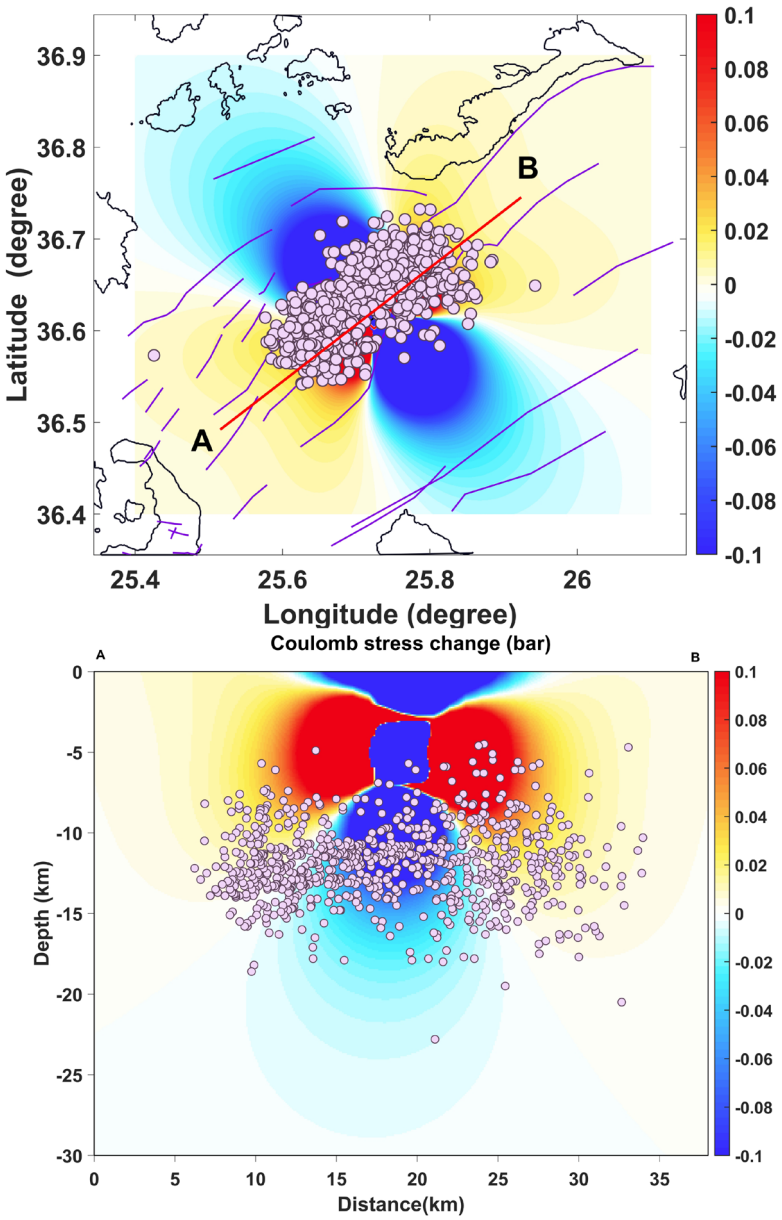

Figure 5. Coseismic Coulomb stress change distributions resulting from the M_w 5.0 earthquake that occurred on 4 February 2025 at 13:04 (UTC), at a focal depth of 5 km. Pink circles denote the hypocenters of swarm events recorded up to 18 February 2025. Cross-section A-B illustrates the depth-dependent variation of ΔCFS.

The Coulomb stress changes analysis focused on the six selected larger seismic events ($M_w \geq 4.8$; Table 2), with the aim of investigating whether static stress redistribution associated with these events may have favored or inhibited subsequent seismic activity during the evolution of the Santorini – Amorgos swarm. The magnitude threshold was adopted in order to focus on the stress perturbations produced by the larger events, which generally affect broader spatial regions than those associated with individual smaller earthquakes. Accordingly, the calculated cumulative ΔCFS represents the combined contribution of the selected source events rather than the total stress redistribution produced by the entire seismic sequence, Although smaller earthquakes were not included as individual stress sources, their collective contribution cannot be excluded. Therefore, the results are interpreted as an assessment of the potential role of Coulomb stress transfer in the progression of the swarm, rather than as evidence of a demonstrated triggering mechanism.

The ΔCFS values were also evaluated at the hypocenters of selected subsequent significant earthquakes (Table 3). Positive Coulomb stress changes were calculated for several of the examined source-receiver earthquake pairs, indicating that the modelled static stress redistribution was favorable to fault activation at these particular

receiver locations. Notably, the M_w 4.8 earthquake of 17 February 2025 at 07:49 (UTC) occurred within a zone that experienced a positive stress change of +1.425 bar induced by the M_w 5.0 event of 4 February 2025. Similarly, positive stress changes were found for the M_w 5.2 earthquake of 10 February 2025 at 20:16 (+0.314 bar) and for the M_w 4.7 event of 7 February 2025 at 07:16 (+0.196 bar), both associated with positive modeled ΔCFS induced by the M_w 5.0 earthquake of 4 February. In addition, the M_w 4.9 earthquake of 10 February 2025 at 22:37 occurred within a region of +0.159 bar generated by the M_w 5.2 event earlier that day. These results are consistent with a possible contribution of static stress transfer to subsequent fault activation at the selected receiver locations. However, they don't establish the relative contribution of this mechanism to the overall evolution or spatial propagation of the swarm.

The sensitivity analysis indicates that ΔCFS remains positive at all selected receiver locations for friction coefficients between $\mu = 0.2$ and 0.6 (Table 3). Although the absolute ΔCFS values vary with the assumed friction coefficient, their sign remains unchanged over the tested range. Thus, for the selected source-receiver pairs, the identification of the receiver locations as positively stressed is robust with respect to this modelling parameter.

For the M_w 5.1 event of 9 February 2025 at 19:05 UTC and the M_w 5.2 event of 10 February 2025 at 20:16 UTC, the calculated ΔCFS distributions exhibit positive stress lobes toward the NE and SW and negative lobes toward the NW and SE (Fig. 6). The earthquake hypocenters are plotted on these stress distributions to show the spatial relationship between seismicity and the modelled static stress changes. The qualitative comparison shows that both the seismicity distribution and the positive ΔCFS lobes are generally aligned with the activated fault system. However, this spatial correspondence alone doesn't establish that static stress transfer controlled the occurrence or migration of the subsequent earthquakes.

Table 3. Calculated Coulomb stress changes (ΔCFS) at the hypocenters of selected subsequent earthquakes induced by preceding source events. ΔCFS values are reported for friction coefficients $\mu = 0.2$, 0.4 and 0.6 to evaluate the sensitivity of the results to the assumed friction coefficient.

Source Event	Subsequent Event	Shear (Δτ)	Normal (Δσ)	Coulomb (ΔCFS) ($\mu = 0.2$)	Coulomb (ΔCFS) ($\mu = 0.4$)	Coulomb (ΔCFS) ($\mu = 0.6$)
03/02/2025 09:29 – M_w 4.8	03/02/2025 12:17 – M_w 4.8	0.055	0.021	0.059	0.063	0.068
03/02/2025 12:17 – M_w 4.8	10/02/2025 20:16 – M_w 5.2	0.018	0.140	0.046	0.074	0.102
04/02/2025 02:46 – M_w 4.7	05/02/2025 19:09 – M_w 5.0	0.073	−0.026	0.068	0.063	0.057
04/02/2025 13:04 – M_w 4.7	07/02/2025 07:16 – M_w 4.7	0.153	0.108	0.175	0.196	0.218
04/02/2025 13:04 – M_w 5.0	10/02/2025 20:16 – M_w 5.2	0.211	0.256	0.262	0.314	0.365
04/02/2025 13:04 – M_w 5.0	17/02/2025 07:49 – M_w 4.8	1.450	−0.064	1.437	1.425	1.412
05/02/2025 19:09 – M_w 5.0	09/02/2025 19:05 – M_w 5.1	0.140	−0.063	0.127	0.115	0.102
10/02/2025 20:16 – M_w 5.2	10/02/2025 22:37 – M_w 4.9	0.129	0.074	0.144	0.159	0.173
10/02/2025 20:16 – M_w 5.2	17/02/2025 07:49 – M_w 4.8	0.140	−0.034	0.133	0.126	0.120
10/02/2025 22:37 – M_w 4.9	18/02/2025 04:46 – M_w 4.9	0.053	0.025	0.058	0.063	0.068

The ΔCFS values were also evaluated at the centroid locations of the 75 earthquake sets 11-75, a subset of the 75 sets used for the Vp/Vs analysis. Sets 1-10 were excluded because they precede the first earthquake included in the stress calculations (M_w 4.8, 3 February 2025, 09:29 UTC). Each set consisted of 15 spatially coherent events, and its centroid was computed from the latitude, longitude, and depth coordinates of the corresponding hypocenters.

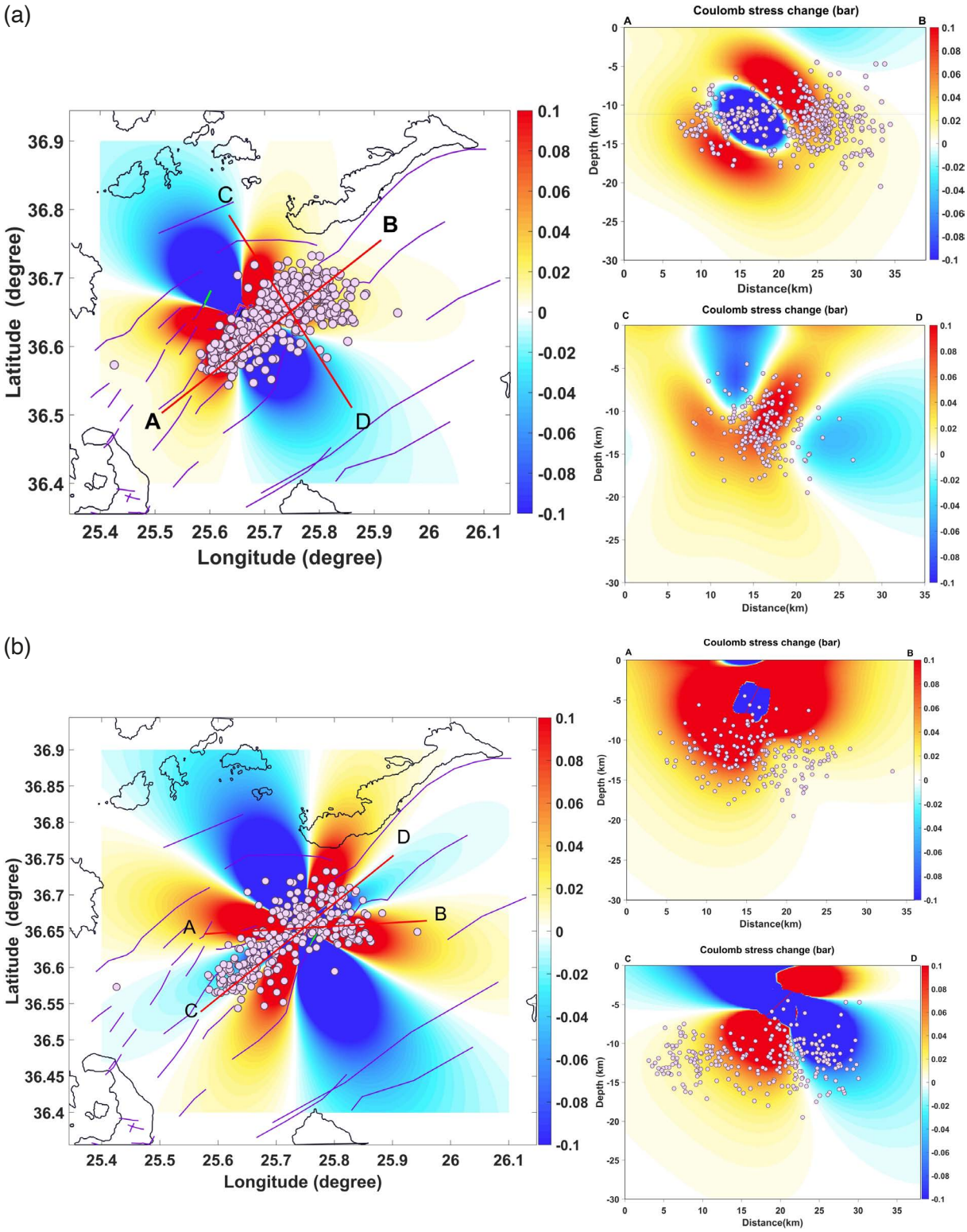

Figure 6. Coseismic Coulomb stress change distributions resulting from the (a) M_W 5.1 and (b) M_W 5.2 earthquakes that occurred on 9 February 2025 at 19:05 (UTC) and 10 February 2025 at 20:16 (UTC), at depths of 11.2 km and 5 km, respectively. Pink circles denote the hypocenters of seismic swarm events recorded up to 18 February 2025. Cross-sections A-B and C-D illustrate the depth-dependent variation of ΔCFS for these earthquakes.

For each centroid, the Coulomb stress changes induced by each of the six selected source earthquakes (Table 2) were calculated, provided that the centroid set occurred after the respective event. The individual ΔCFS contributions were then summed to obtain the cumulative Coulomb stress change for each set, with positive values indicating stress loading and negative values indicating stress shadowing.

The spatial distribution of cumulative ΔCFS is shown on Fig. 7. Each circle represents the centroid of a set, with its size indicating the cumulative ΔCFS class and its color scaled according to the sequential set index. Positive and negative values (in bar) indicate stress loading and stress shadowing, respectively, at the sampled centroid locations. These values were mapped using ArcMap 10.6 to illustrate their spatial distribution across the Santorini-Amorgos fault system.

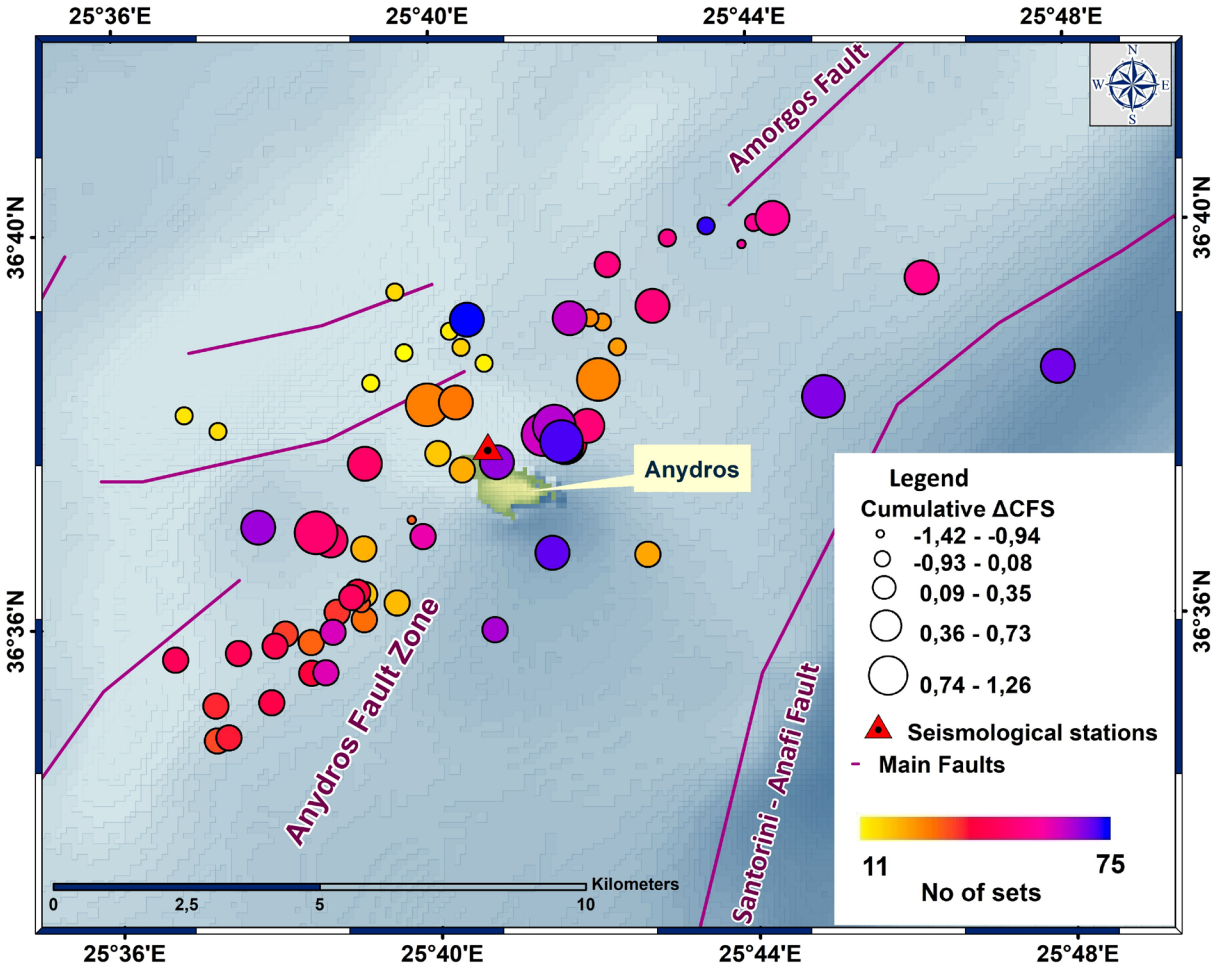

Figure 7. Spatial distribution of cumulative Coulomb stress changes (ΔCFS, in bar) induced by the six selected larger earthquakes ($M_w \geq 4.8$; Table 2), evaluated at the centroid locations of earthquake sets 11-75. Major NE-SW trending fault traces are shown in purple (Ganas, 2025).

The cumulative ΔCFS at the centroid of each earthquake set was plotted against the mean occurrence time of that set (Fig. 8). This representation provides the stress estimates associated with the sets used in the Vp/Vs analysis. However, successive points correspond to different locations as well as different times. Variations therefore reflect both spatial differences in the stress field and the accumulation of contributions from preceding modelled earthquakes. A two-point moving average was calculated in Excel and is shown only as a visual guide to the set-specific ΔCFS values.

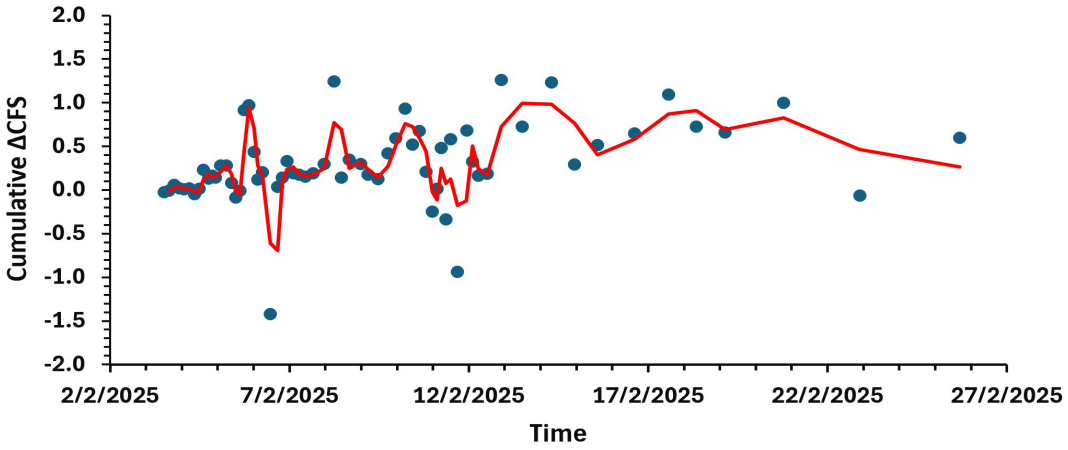

Figure 8. Cumulative Coulomb stress change (ΔCFS, in bar) evaluated at the centroids of earthquake sets 11-75, plotted against their mean occurrence times. Blue dots represent individual set-specific values, and the red line represents a moving average with a period of 2 (averaging two consecutive set-specific values), calculated and included as a visual guide.

5. Vp/Vs ratio Variations – Wadati Method

5.1 Results for the time period January 2011-June 2025

The P- and S-wave arrival times of waveform data recorded at 21 Hellenic Unified Seismological Network (HUSN) stations were selected from January 2011 to June 2025 (Evangelidis et al., 2021). In total, more than 2,000 manually revised events by the Seismological Laboratory of the National and Kapodistrian University of Athens (SL-NKUA) were used within the above-mentioned period in the hypocenter determination. This study employed the HYPOINVERSE code for the hypocenter location of the available events (Klein, 2002) using a local 1-D velocity model for the area of Santorini-Amorgos (Karakonstantis and Vallianatos, 2024).

A dataset of relatively well-constrained events was selected, using an azimuthal gap smaller than 200° and an RMS residual below 0.75 s for all time windows. To ensure a reliable assessment of the Vp/Vs ratio, the phase file was divided into three distinct temporal intervals: the 2011-2012 seismicity (Fig. 9), the intermediate period of relative quiescence between 2015 and May 2024 (Fig. 10), during which only minor activity occurred near Kolumbo, and the period of unrest affecting the Santorini caldera and the Amorgos basin from September 2024 to June 2025 (Fig. 11).

Next, the study area was subdivided into two regions: the intracaldera domain and the Kolumbo-Amorgos basin. For the 2011-2012 interval, the intracaldera region included 1,114 earthquakes with 15,361 pairs of P and S-arrival picks, while the Kolumbo-Amorgos basin contained 363 events with 2,044 P and S pair of picks respectively. During the 2015-May 2024 interval, seismicity was limited to the Kolumbo-Amorgos basin, where 372 events were recorded, yielding 3,584 pairs of P and S-arrival picks. Finally, for the September 2024-June 2025 interval, the intracaldera region comprised 272 events with 2,316 pair of P and S wave arrival-times, whereas the Kolumbo-Amorgos basin included 950 earthquakes with 10,059 pairs of P and S wave picks respectively.

A Wadati diagram (Wadati and Oki, 1933; Kisslinger and Engdahl, 1973; Diehl et al., 2009) was used to calculate the Vp/Vs ratio of the earthquakes, which varied in both space and time (calculated by linear least squares). Furthermore, S picks with S-P travel time differences larger than 5 s off the main trend were removed (~0.09% of the phase file). The resulting values of Vp/Vs vary between 1.72 and 1.77, for the selected sub-areas in the different time periods. The plots were made for all the time periods for the area of Kolumbo-Amorgos, while in the intracalderic area, the plots were feasible mainly in the time span of 2011-2012 and June 2024 to June 30, 2025.

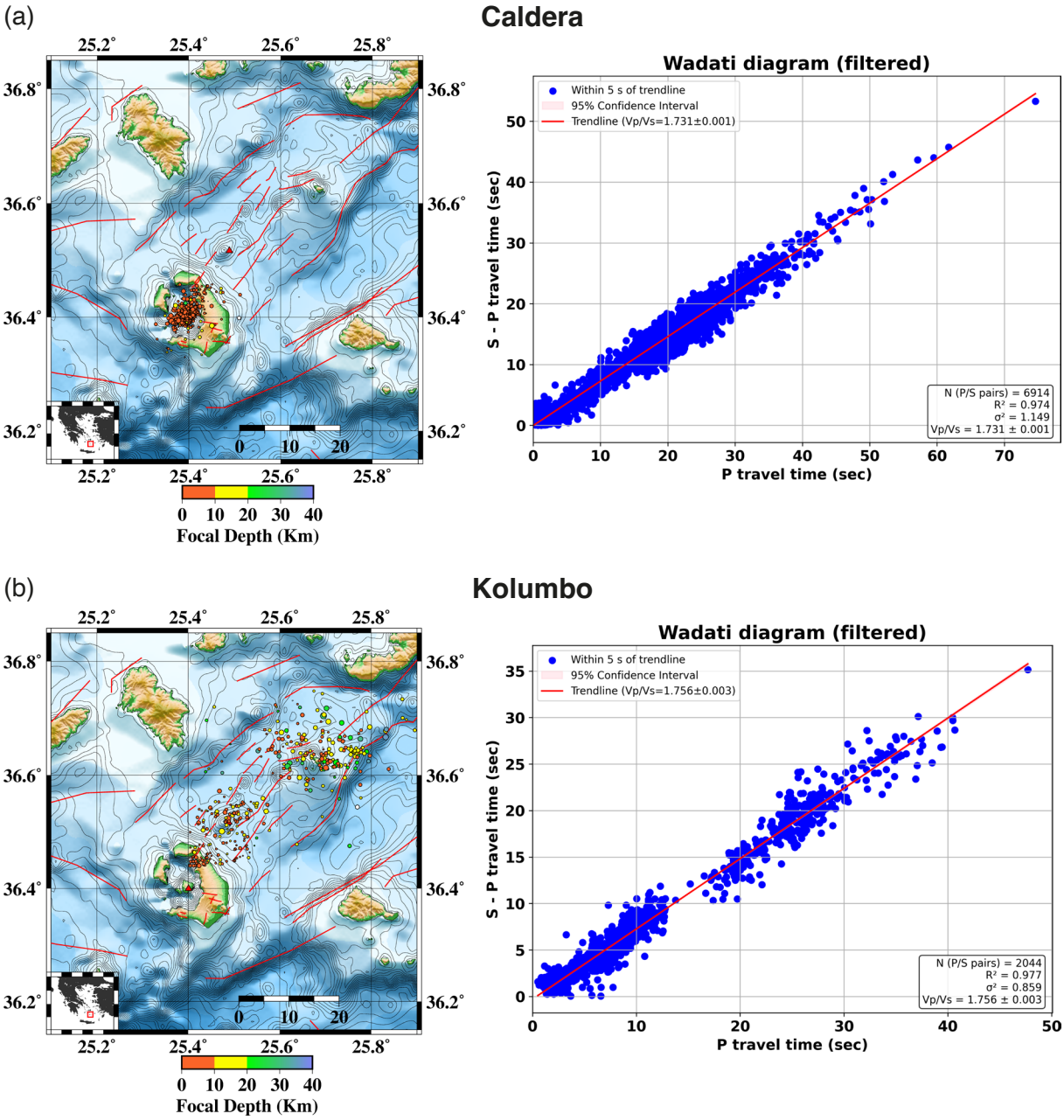

Figure 9. Results for the time window of the 2011-12 seismic crisis and (a) the seismic events in the caldera (left) used for the Wadati plot (right) and (b) the respective epicenters of the earthquakes in the Kolumbo-Amorgos basin (left) used for the Wadati plot (right). The reported ± values indicate the regression-derived uncertainties of the Vp/Vs estimates, and the shaded bands represent the 95% confidence intervals of the fitted regression lines.

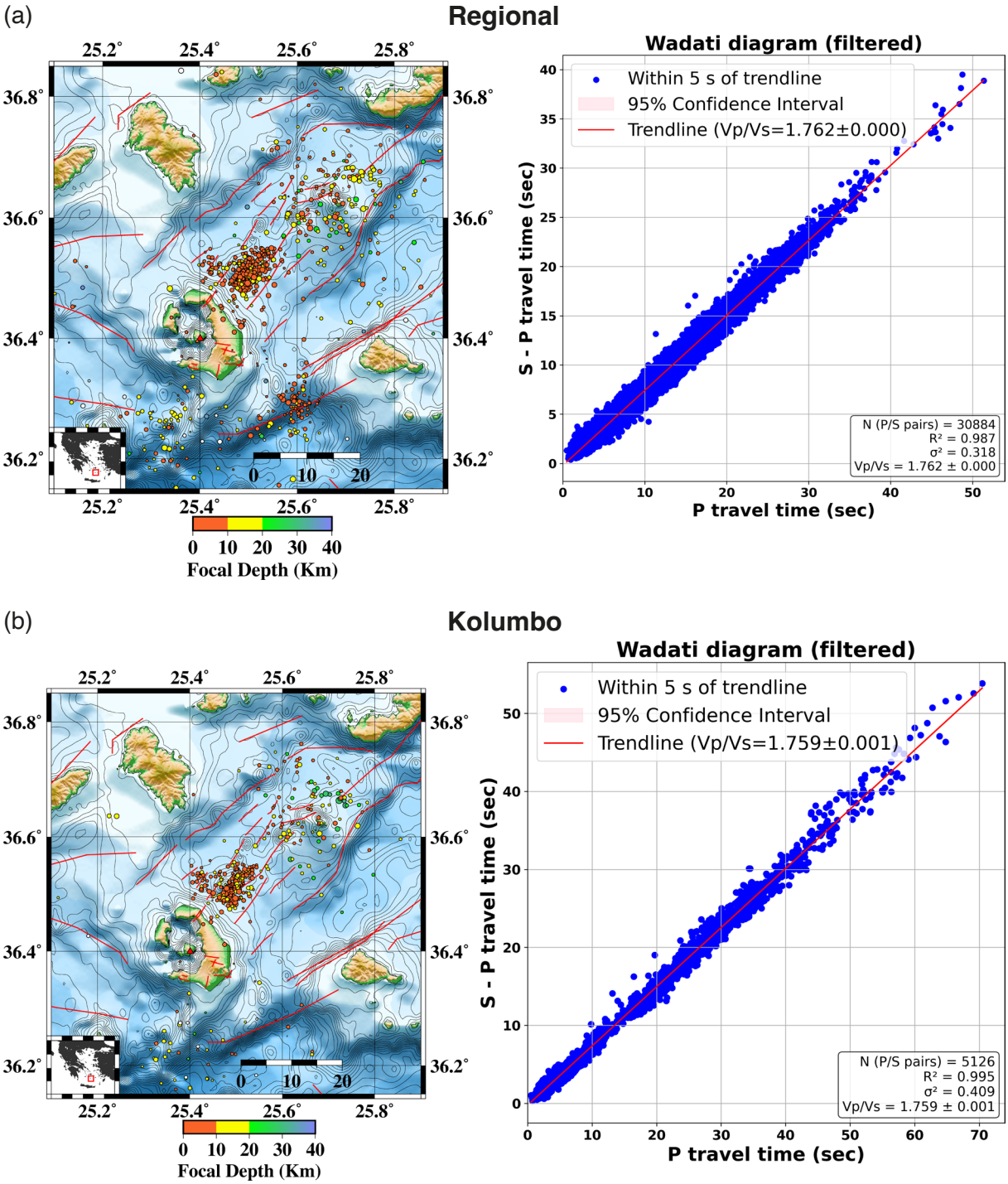

Figure 10. Results for the time window of the 2015-May 2024 and (a) the seismic events in the broader area of the Santorini Island Volcanic Complex and the neighboring areas (left) used for the Wadati plot (right) and (b) the respective epicenters of the earthquakes in the Kolumbo-Amorgos basin (left) used for the Wadati plot (right). The reported ± values indicate the regression-derived uncertainties of the Vp/Vs estimates, and the shaded bands represent the 95% confidence intervals of the fitted regression lines.

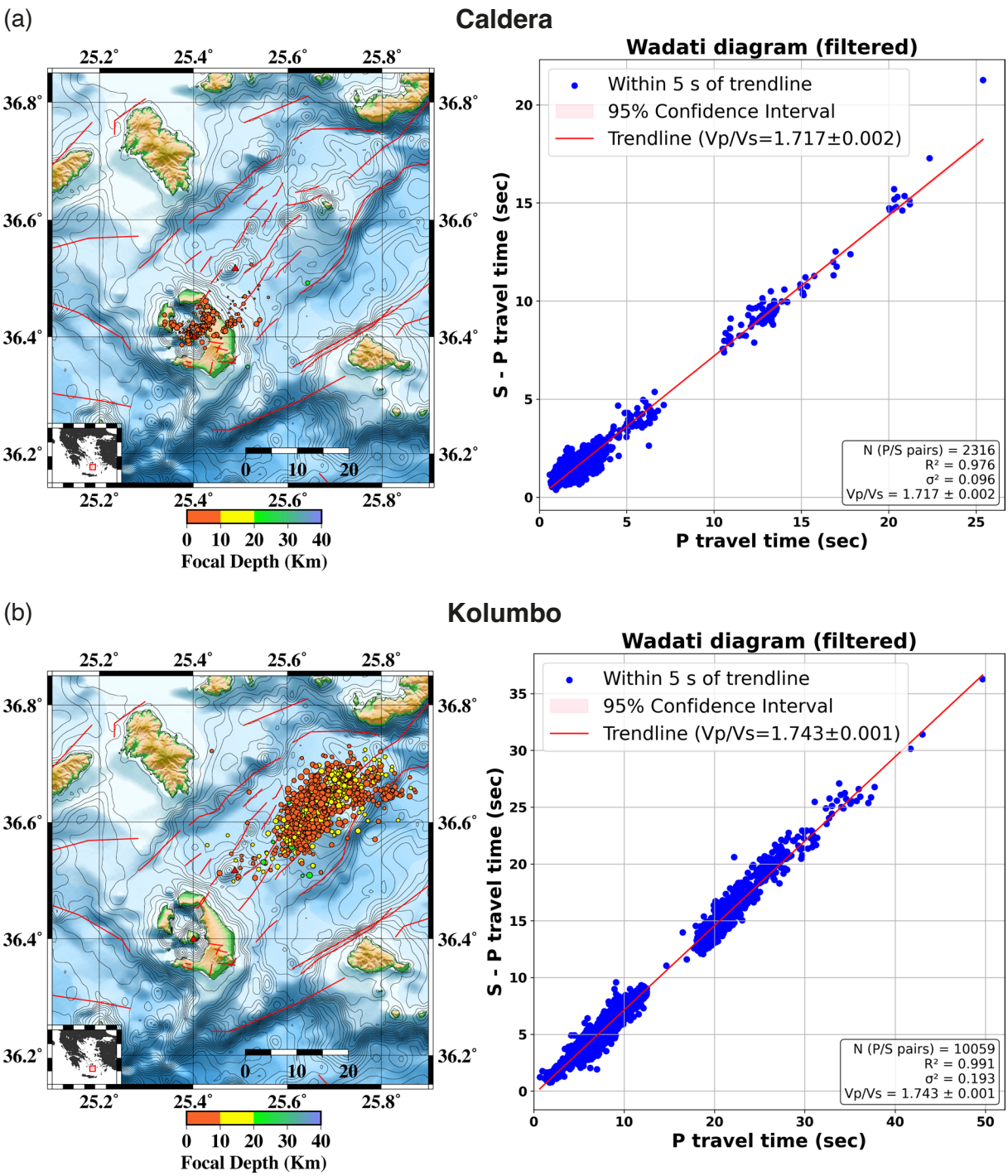

Figure 11. Results for the one-year time window between (June 2024-June 2025) and (a) the seismic events in the caldera (left) used for the Wadati plot (right) and (b) the respective epicenters of the earthquakes in the Kolumbo-Amorgos basin (left) used for the Wadati plot (right). The reported ± values indicate the regression-derived uncertainties of the Vp/Vs estimates, and the shaded bands represent the 95% confidence intervals of the fitted regression lines.

5.2 Results for the period January 25-March 10, 2025

The temporal and spatial variations of the Vp/Vs velocity ratio were examined for the period January 25 to March 4, 2025, as this ratio may provide indirect information on changes in the physical properties of the seismogenic medium, potentially associated with variations in pore-fluid conditions during seismic activity (Masihi and Fischer, 2025). Formal regression-derived uncertainty estimates are not available for the individual set-specific

Vp/Vs values shown in Fig. 12b, because the retained calculation output contains the final Vp/Vs estimates but not the regression standard errors required to reconstruct confidence intervals. Consequently, the temporal variations shown in Fig. 12b are interpreted descriptively, and differences between individual consecutive estimates are not considered statistically significant.

The set-based Vp/Vs analysis was performed using 1.125 earthquakes, organized into 75 consecutive, non-overlapping sets of 11 events each, following the spatial selection procedure described in Section 3.

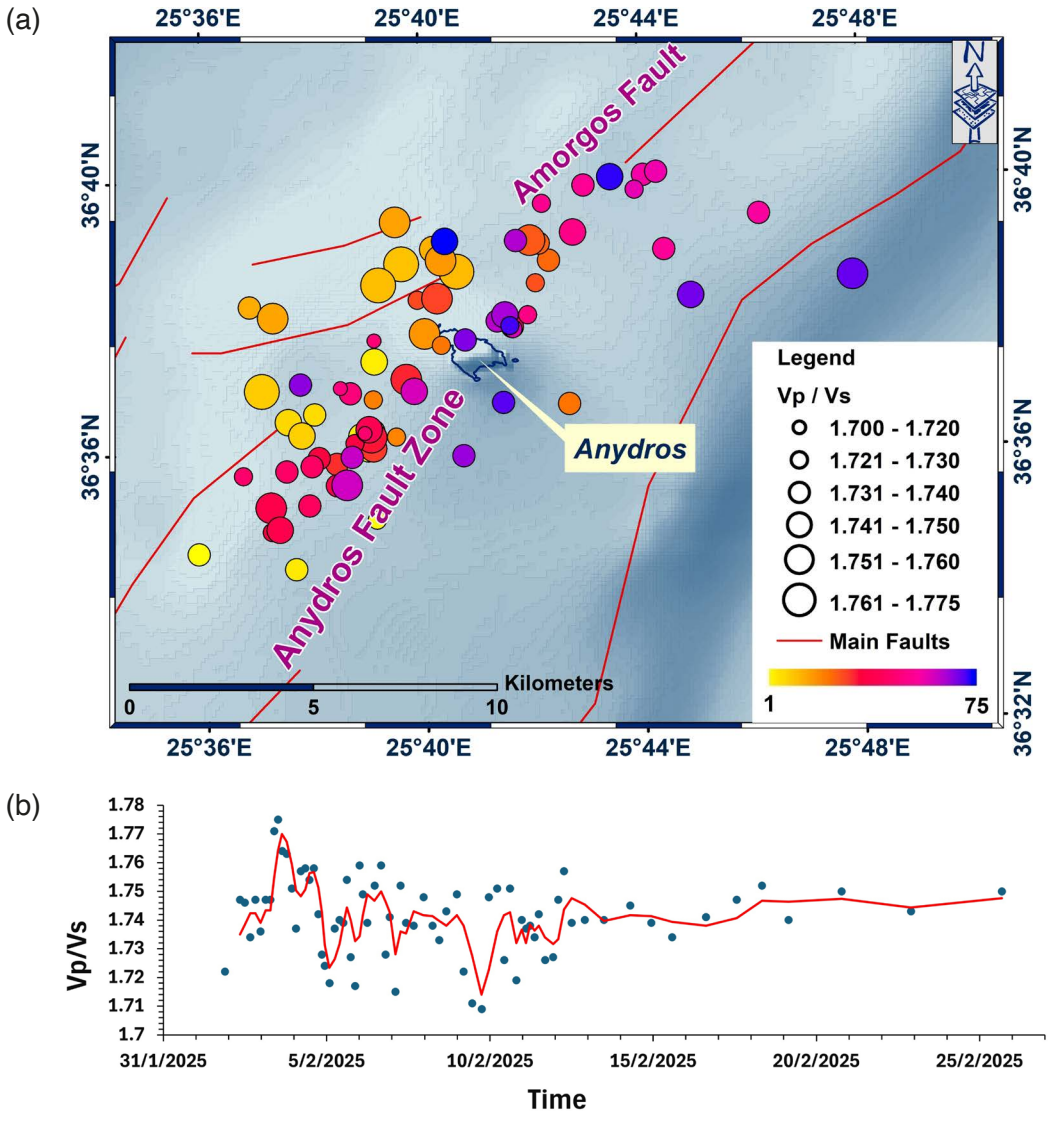

Figure 12. (a) Spatial distribution of Vp/Vs values. Each dataset is represented by a circle plotted at the centroid of the polygon defined by the epicenters of its 15 associated earthquakes. Circle size is proportional to the estimated Vp/Vs value, while color corresponds to the sequential set index (1-75). (b) Temporal evolution of set-specific Vp/Vs estimates obtained using the Wadati method for the early 2025 Santorini-Amorgos seismic swarm. Blue circles denote individual Vp/Vs estimates, while the red line shows a two-point moving average included only as a visual guide. Formal confidence intervals are not available for the individual set-specific estimates; therefore, the temporal pattern is interpreted descriptively.

The set-specific Vp/Vs estimates show temporal variability during the swarm, ranging from approximately 1.70 on 9-10 February 2025 to approximately 1.78 on 3 February 2025, with regression coefficients of determination $R^2 \geq 0.98$. The point estimates show an initial increase toward the value observed on 3 February, followed by variability and an overall decrease toward the lower values recorded on 9-10 February. Subsequently, smaller variations are observed, with values tending toward approximately 1.74-1.75 later in the observation period (Fig. 12).

Because formal uncertainty estimates are not available for the individual set-specific Vp/Vs values, the statistical significance of differences between consecutive estimates cannot be evaluated. The observed temporal pattern may reflect changes in the physical properties of the seismogenic medium, although the underlying physical mechanism cannot be uniquely identified from Vp/Vs variations alone (Masihi and Fischer, 2025).

6. Spatial Distribution and Temporal Evolution of the Maximum Seismicity Rate (λ_{max})

To investigate spatial variations in seismicity rate along the activated Santorini-Amorgos seismogenic zone, earthquake epicenters were projected onto a rotated coordinate system aligned with the strike of the activated structure. The transformation was performed using a rotation angle of 40° relative to the geographic reference frame, with the rotation reference point defined by the mean epicentral coordinates of the first ten events in the catalog. In the rotated system, the X-axis corresponds to the along-strike direction, whereas the Y-axis represents the across-strike direction. Only earthquakes located within ±5 km of the central along-strike axis were retained, defining a study corridor approximately 10 km wide. This corridor was subsequently subdivided into consecutive 2-km-wide spatial zones along strike (Fig. 13).

Each zone represents a discrete segment of the activated seismogenic zone, encompassing all earthquakes within the corresponding along-strike interval. The geometry and numbering of the spatial zones are shown in Figure 13, and the total number of events within each zone during the study period is reported in Table 4.

For each spatial zone, an independent earthquake subcatalog was compiled, containing only the events located within the corresponding along-strike interval. The temporal evolution of seismic activity in each zone was quantified using the seismicity-rate function:

$$\lambda(t) = \frac{\Delta N}{\Delta t} \tag{2}$$

where N is the number of earthquakes occurring within the time interval Δt. The seismicity rate was calculated independently for each spatial zone using 6-hour time bins throughout the study period. Consequently, each $\lambda(t)$ curve describes the temporal evolution of seismic activity within a specific segment of the activated seismogenic zone (Fig. 14).

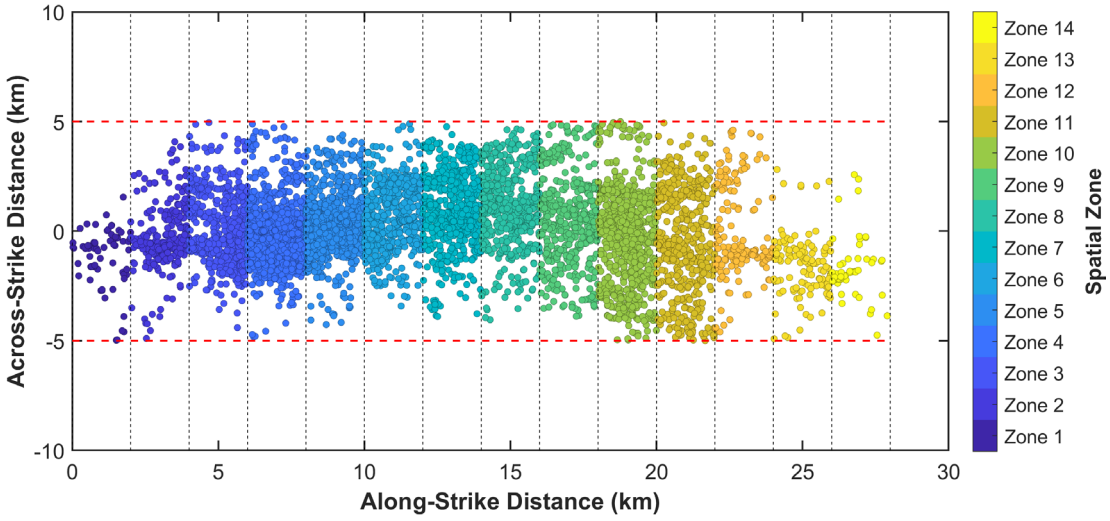

Figure 13. Spatial distribution of seismicity in the rotated coordinate system used for spatial analysis. The X-axis corresponds to the along-strike direction of the activated seismogenic zone, and the Y-axis to the across-strike direction. Red dashed lines delineate the boundaries of the selected seismogenic corridor (±5 km from the central axis). The colored 2 km-wide zones represent the segments used to analyze spatial variability and to calculate the maximum seismicity rate λ_{max}. The total number of events in each zone is reported in Table 4.

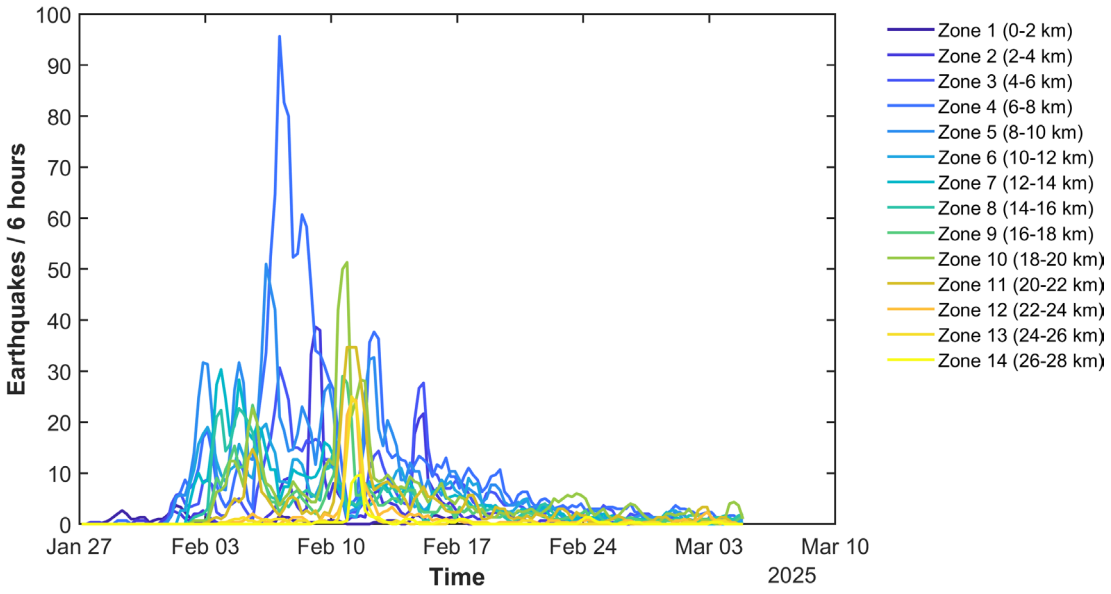

Figure 14. Temporal evolution of the seismicity rate $\lambda(t) = \Delta N/\Delta t$, calculated independently for each 2 km-wide spatial zone of the activated Santorini-Amorgos seismogenic zone. Each curve corresponds to a distinct along-strike segment of the selected area.

The resulting seismicity-rate curves are presented in Figure 14, where each curve corresponds to a distinct spatial zone computed exclusively from earthquakes within the respective interval. For each zone, the maximum seismicity rate λ_{max} was determined as $\lambda_{max} = \max\left(\frac{\Delta N}{\Delta t}\right)$.

Table 4. Total number of earthquakes, maximum seismicity rate (λ_{max}) and the corresponding time of maximum activation ($T(\lambda_{max})$) for each spatial zone (2 km along strike × 10 km across strike) within the rotated Santorini-Amorgos seismogenic area.

Zone ID	No of events	$T_{(\lambda max)}$	λ_{max}
1	70	1/2/2025 09:00	3.7
2	399	9/2/2025 03:00	38.6
3	788	7/2/2025 03:00	30.7
4	1675	7/2/2025 03:00	95.7
5	1225	6/2/2025 09:00	51
6	692	6/2/2025 09:00	19.7
7	726	3/2/2025 21:00	30.3
8	545	4/2/2025 21:00	22.7
9	505	10/2/2025 15:00	29
10	816	10/2/2025 21:00	51.4
11	519	10/2/2025 21:00	34.6
12	178	11/2/2025 09:00	24.2
13	129	11/2/2025 03:00	25.1
14	53	11/2/2025 15:00	9.7

The time $T_{(\lambda max)}$ was assigned to the midpoint of the 6-hour bin in which the maximum seismicity rate was observed. Each spatial zone was therefore characterized by two parameters: (i) the maximum seismicity rate, λ_{max}, and (ii) the corresponding time of maximum seismic activation, $T_{(\lambda max)}$. $T_{(\lambda max)}$ represents the center time of the 6-hour bin at which the maximum seismicity rate was attained, whereas λ_{max} quantifies the highest level of seismic activity recorded within a given spatial zone during the study period. Accordingly, λ_{max} provides a measure of the maximum local seismic activation developed within each segment of the activated seismogenic zone. Because $T_{(\lambda max)}$ is assigned to the midpoint of a 6-hour bin, its temporal resolution is ± 3 h.

7. Temporal Evolution of the Spatial Fractal Correlation Dimension

The spatial fractal correlation dimension, D_c, characterizes the scaling of the earthquake hypocentral distribution through the relationship between the correlation integral and inter-event distances (Kagan and Knopoff, 1980; Grassberger and Procaccia, 1983a, 1983b). Higher and lower D_c values describe higher and lower dimensional spatial distributions, respectively, over the selected scaling range. D_c doesn't measure the physical size or volume occupied by the hypocenters. Here, its temporal variation is used to describe changes in the spatial organization of seismicity.

The correlation integral method of Grassberger and Procaccia (1983a, b) provides a robust framework for quantifying the spatial clustering of earthquake hypocentres. For a seismic sequence, the spatial correlation integral C(r) measures the proportion of earthquake pairs with hypocentral separation less than a given distance r, thereby describing the spatial organization of seismicity within the activated fault-fracture network:

$$C(r) = \frac{2}{N(N-1)} \sum_{j=1}^{N-1} \sum_{i=j+1}^{N} H\left(r - r_{ij}\right) \tag{3}$$

where N is the number of earthquakes in the analyzed window, r_{ij} is the correlation distance, defined here as the three-dimensional Euclidean distance between events i and j, H is the Heaviside step function, and r is the spatial scale length.

For a fractal spatial distribution, the correlation integral follows a power-law scaling relation, $C(r) \propto r^{Dc}$, where D_c is estimated from the slope of the linear part of the $\log C(r)$ versus $\log r$ curve:

$$D_c = \frac{d \log C(r)}{d \log r} \tag{4}$$

To investigate the temporal evolution of spatial clustering, D_c was estimated using a moving-window approach. Each window contained 600 consecutive earthquakes and was advanced by 80 events, with the resulting D_c values assigned to the central time of each window.

Hypocentral locations were converted to Euclidean distances, given as:

$$r_{ij} = \sqrt{\left(x_i - x_j\right)^2 + \left(y_i - y_j\right)^2 + \left(z_i - z_j\right)^2}, \tag{5}$$

where $x_i, y_i, z_i, x_j, y_j, z_j$ denote the Euclidean coordinates of the i-th earthquake respectively. Geographic coordinates were converted to kilometers, and focal depth was incorporated as the third spatial dimension.

The correlation integral was evaluated at logarithmically spaced distance scales. The scaling region was identified automatically by searching for the most linear segment in $\log C_r$ versus $\log r$ space. To reduce distortions from location uncertainties and saturation effects, the first and last three scale values were excluded. Linear regressions were fitted to candidate segments of 8-15 consecutive points, and the optimal scaling interval was selected using a combined criterion based on the coefficient of determination R^2, root mean square error (RMSE), and the number of fitted points (Grassberger and Procaccia, 1983a, 1983b).

The uncertainty of each D_c estimate was quantified from the linear regression used to determine the slope of the $\log C(r)$-$\log r$ relation within the selected scaling interval. The standard error of the fitted slope was calculated, and a two-sided 95% confidence interval was obtained using the Student-t distribution with n-2 degrees of freedom, where n is the number of points included in the fitted scaling range. In addition, a residual bootstrap analysis with 100 realizations was performed as a robustness check. These uncertainty estimate quantify the uncertainty associated with the regression within the selected scaling interval; they don't constitute a full propagation of uncertainties in hypocentral locations or in the selection of the scaling region.

The resulting $D_c(t)$ series describes changes in the estimated correlation dimension of successive hypocentral distributions. These changes are interpreted in terms of spatial organization over the fitted scaling ranges, without inferring expansion or contraction of the volume occupied by the earthquakes.

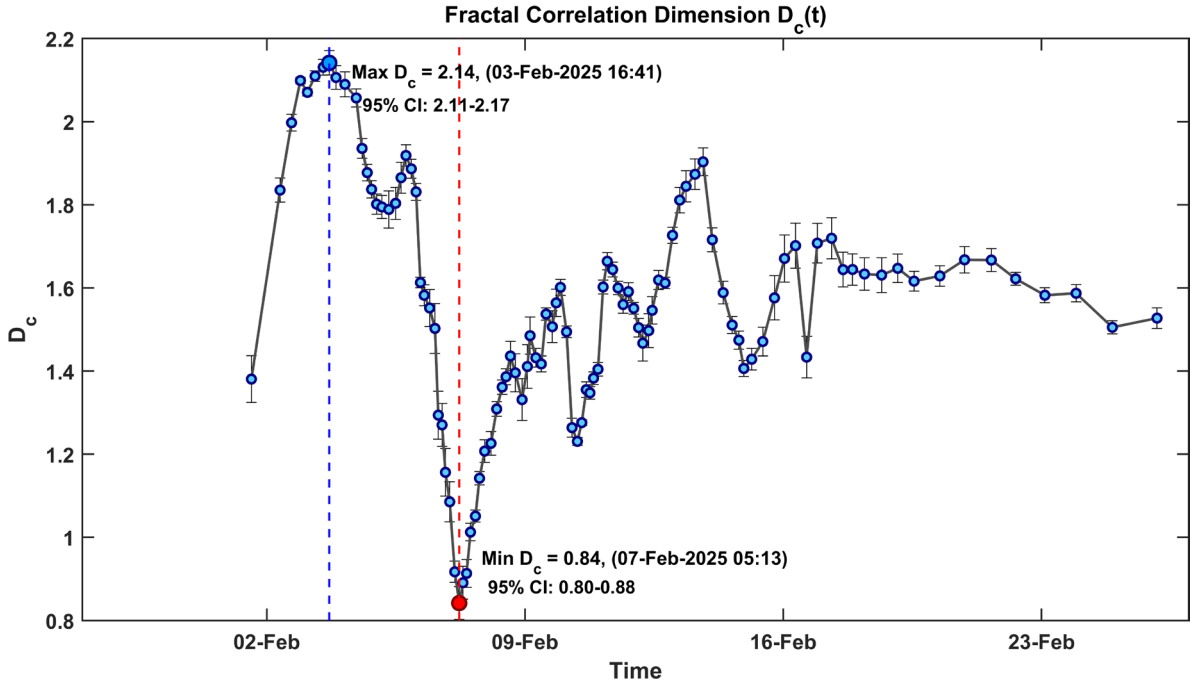

Figure 15. Temporal evolution of the spatial fractal correlation dimension D_c during the 2025 Santorini-Amorgos seismic sequence. D_c was computed using three-dimensional Euclidean distances in moving windows of 600 successive earthquakes with a step of 80 events. Values are plotted at the central time of each window. Black error bars indicate the regression-derived 95% confidence intervals of the D_c estimates. The maximum D_c value is 2.14 (95% CI: 2.11-2.17), whereas the minimum is 0.84 (95% CI: 0.80-0.88).

Figure 15 illustrates the temporal evolution of D_c during the 2025 Santorini-Amorgos seismic sequence. Early in the sequence, D_c increased from approximately 1.4 to a maximum value of 2.14 (95% CI: 2.11-2.17) on 3 February 2025, indicating a shift towards a higher-dimensional hypocentral distribution over the fitted spatial scales.

Between 6 and 7 February, D_c decreased, reaching a minimum value of 0.84 (95% CI: 0.80-0.88) on 7 February 2025. The magnitude of this decrease is substantially larger than the regression-derived uncertainty of the individual D_c estimates. This decrease indicates a shift towards a lower-dimensional spatial distribution but does not by itself establish a reduction in the volume occupied by the hypocenters or identify the orientation of the structures hosting the earthquakes.

Following this minimum, D_c increased to approximately 1.3-1.7, with a secondary maximum around 12-13 February. During the remainder of the sequence, values remained relatively stable between 1.5 and 1.7. This recovery indicates a return to higher correlation-dimension values, rather than necessarily an expansion of the hypocentral distribution.

Overall, the D_c series records an initial increase, a pronounced minimum on 6-7 February, and a subsequent recovery. These variations characterize changes in the spatial organization of seismicity over the analyzed scales. The later values are not interpreted as a background level for the region, since an equivalent analysis of preceding seismicity wasn't performed.

8. Discussion

The 2025 Santorini-Amorgos seismic swarm offers an opportunity to investigate the relationship between stress transfer, temporal variations in the Vp/Vs ratio, and changes in the spatial organization of seismicity.

Coulomb stress modelling reveals positive and negative stress changes around the modelled rupture planes (Fig. 4-6). Positive ΔCFS values were also calculated at the hypocenters of several selected subsequent earthquakes (Table 3). These results are consistent with a possible contribution of static stress transfer to subsequent fault activation. Similar relationships between positive Coulomb stress changes and subsequent seismicity have been reported by King et al. (1994), Stein (1999), and Kilb et al. (2002). However, the present analysis doesn't establish a statistically significant association between positive ΔCFS and the overall spatial distribution of subsequent seismicity.

A potential limitation of the Coulomb stress analysis arises from the geometric relationship between the modelled stress field and the spatial distribution of seismicity. In Figs. 4-6, the positive ΔCFS lobes are generally aligned with the strike direction of the activated fault system, which also corresponds to the predominant orientation of seismicity. Consequently, the apparent spatial correspondence between positive Coulomb stress changes and earthquake locations may partly reflect the underlying fault geometry rather than a direct triggering effect of static stress transfer. This geometric bias limits the interpretation of the spatial overlap between seismicity and positive ΔCFS regions as independent evidence of earthquake triggering. Although positive ΔCFS values calculated at the hypocenters of selected subsequent earthquakes are consistent with conditions favouring fault activation, they don't establish that static stress transfer was the dominant mechanism controlling the evolution of the swarm.

Static Coulomb stress transfer may have contributed to the evolution of the seismic sequence by favouring fault activation at selected locations where positive ΔCFS values were calculated. However, its relative contribution to the overall development of the swarm cannot be established from the present analysis. In addition to the potential geometric bias discussed above, the Coulomb modelling accounts for static tress changes induced by the selected source earthquakes, whereas seismic swarms in volcanic-tectonic settings may also be influenced by aseismic deformation, pore-pressure diffusion, permeability changes, small unresolved events, and uncertainties in fault geometry and slip distribution (Cocco and Rice, 2002; Chen et al., 2012; Hainzl et al., 2006). The sensitivity test for $\mu = 0.2$-0.6 further shows that the positive sign of ΔCFS at the selected receiver locations is preserved across the tested friction range Nevertheless, the absolute ΔCFS values remain model dependent, because uncertainties in focal-mechanism parameters, source depth, rupture geometry and dimensions, and slip distribution were not explicitly propagated. Therefore, positive ΔCFS should be interpreted as a condition potentially favorable to earthquake triggering rather than as conclusive evidence of the mechanism controlling the sequence.

The temporal evolution of the Vp/Vs estimates shows marked variability during the swarm. The observed values ranged from approximately 1.70 to 1.78, with the highest point estimates recorded during the most active stage of the sequence. Formal uncertainty estimates are not available for the individual set-specific Vp/Vs values, and therefore the statistical significance of differences between consecutive estimates cannot be assessed. Nevertheless, the overall temporal pattern may reflect changes in the physical properties of the seismogenic zone. Since Vp/Vs is sensitive to pore-fluid conditions, the observed variability may be consistent with transient changes in fluid distribution and pore pressure during the swarm, although this interpretation remains non-unique (Masihi and Fischer, 2025).

The subsequent decrease and stabilization of Vp/Vs estimates may be consistent with transient changes in pore-fluid pressure, fluid redistribution, or progressive drainage along the activated fault-fracture network. However, these mechanisms cannot be independently distinguished from the available observations. Therefore, the observed Vp/Vs variability is interpreted as a possible indication of fluid-related processes rather than direct evidence of fluid migration (Chen et al., 2012; Hainzl et al., 2006).

The temporal behavior of D_c provides complementary information on the spatial organization of earthquake hypocenters. Values above 2 early in the sequence were followed by a decrease to a minimum of 0.84 (95% CL: 0.80-0.88) on 6-7 February and a subsequent recovery. This pattern suggests a transition from a higher to a lower dimensional distribution and then back towards higher dimensional organization over the analyzed scales. Although ideal planar and linear distributions have dimensions of 2 and 1, respectively, the estimated D_c values alone don't uniquely establish fault geometry or orientation. No inference about changes in the occupied spatial volume is made from D_c. Comparison with the background seismicity preceding the 2025swarm would be valuable for establishing the characteristic range of the region and assessing the significance of the observed changes.

The four parameters examined in this study (ΔCFS, Vp/Vs, D_c, and λ_{max}) were calculated using different spatial and temporal subsets according to their specific methodological requirements. Consequently, a direct quantitative

correlation between the four parameters wasn't performed. Their combined interpretation is therefore restricted to a complementary qualitative assessment of the seismic sequence, rather than establishing a direct relationship between their temporal or spatial variations. A systematic comparison based on common spatiotemporal subsets would be required to further investigate possible correlations between these parameters.

The Anydros area appears to have played a key role in the evolution of the swarm. Rather than acting only as a passive geographic sector between Santorini and Amorgos, it likely represents a structurally favourable part of the offshore fault-fracture system where stress loading, permeability pathways, and earthquake clustering interacted (Nomikou et al., 2013; Ganas, 2025; Zaccagnino et al., 2025). The spatial distribution of seismicity provides the geographical context for discussing the role of the Anydros region (Fig. 1). The D_c series describes changes in hypocentral spatial organization (Fig. 15) but doesn't by itself locate these changes within a particular part of the offshore fault system or demonstrate a mechanical or hydraulic connection.

Compared with the 2011-2012 Santorini unrest, which was mainly expressed within the Santorini volcanic system and did not culminate in an eruption, the 2025 sequence was characterized by pronounced offshore migration toward the Santorini-Amorgos zone and by strong reorganization of hypocentral clustering (Vallianatos et al., 2013; Papadimitriou et al., 2015; Kaviris et al., 2015; Zaccagnino et al., 2025). This difference suggests that the 2025 swarm was not only a caldera-centered episode of volcanic unrest but involved the broader volcanic-tectonic fault system between Santorini, Kolumbo, Anydros, and Amorgos. Similar to interpretations proposed for other seismic swarms, the evolution of the Santorini-Amorgos sequence may involve both static stress redistribution and transient fluid-related processes, although their individual contributions and possible interactions cannot be quantitatively established from the present analysis (Chen et al., 2012; Michas et al., 2022; Srijayanthi et al., 2022). The coexistence of positive Coulomb stress changes at selected receiver locations, Vp/Vs variability, and marked temporal changes in D_c is consistent with the possible involvement of multiple processes in the evolution of the swarm. Static stress redistribution may have favoured local fault activation, while fluid-related processes and changes in fault-network permeability may also have contributed to the persistence and migration of the seismicity.

The combined observations suggest that the Santorini-Amorgos swarm evolved through successive phases of spatial reorganization. Temporal variations in Vp/Vs and D_c indicate changes in the physical properties and spatial organization of the seismogenic zone, although their relationship cannot be uniquely established from the present analysis. Positive ΔCFS values calculated at selected receiver locations are consistent with a possible contribution of static stress transfer to fault activation. However, the geometric bias associated with the orientation of the activated fault system and the absence of a quantitative assessment of the spatial association between ΔCFS and seismicity prevent a definitive evaluation of the relative contributions of stress transfer and fluid-related processes to the evolution of the swarm.

9. Concluding Remarks

This study examined the evolution of the 2025 Santorini-Amorgos seismic swarm through an integrated analysis of Coulomb stress transfer, temporal variations of the Vp/Vs ratio derived from the Wadati method, and the evolution of the spatial fractal correlation dimension D_c. The combined results provide a complementary interpretation of the evolution of the seismogenic system, consistent with the possible involvement of both mechanical and fluid-related processes, without demonstrating a direct quantitative relationship among the examined parameters.

Coulomb stress modelling identified positive and negative stress changes associated with the strongest earthquakes of the sequence. Positive ΔCFS values were calculated at the hypocenters of several selected subsequent earthquakes, indicating that static stress redistribution may have favoured fault activation at these locations. However, the spatial correspondence between positive ΔCFS lobes and seismicity may partly reflect the underlying fault geometry. Consequently, the present analysis doesn't establish the proportion of subsequent earthquakes occurring within positive stress regions or the relative contribution of static stress transfer to the overall evolution of the swarm.

The Vp/Vs ratio exhibited temporal variability, ranging from about 1.70 to 1.78 during the swarm. These fluctuations may reflect changes in the physical properties of the seismogenic medium and could be consistent with transient fluid-related processes. However, because formal uncertainties are not available for the individual set-specific Vp/Vs estimates, differences between consecutive values are interpreted descriptively, and their statistical significance cannot be assessed.

The spatial fractal correlation dimension, D_c, displayed pronounced temporal variations. Values above 2 early in the sequence reached a maximum of 2.14 (95% CI: 2.11-2.17) and subsequently decreased to a minimum of 0.84 (95% CI: 0.80-0.88) on 7 February 2025, before recovering to approximately 1.5-1.7 later in the study period. This pattern indicates changes in the dimensional character of the hypocentral distribution over the analyzed spatial scales. It does not establish corresponding changes in the spatial volume occupied by the earthquakes.

Taken together, the results of the Coulomb stress modeling, Vp/Vs analysis and spatial fractal correlation dimension, D_c, analysis are consistent with the possible involvement of multiple processes during the 2025 Santorini-Amorgos seismic swarm. Static stress redistribution may have favoured fault activation at selected locations, while the observed Vp/Vs variability and changes in D_c provide complementary information on the evolving physical properties and spatial organization of seismicity. However, the relative contributions of static stress transfer and fluid-related processes cannot be uniquely determined from the present analysis. Furthermore, the four parameters were not evaluated using common spatiotemporal subsets, so their combined interpretation remains qualitative. These findings highlight the value of integrating complementary seismological methods while acknowledging the limitations associated with the interpretation of individual parameters.

Data availability statement. Data used in this work are presented in "Fountoulakis, I. and C. P. Evangelidis (2025). The 2024-2025 seismic sequence in the Santorini-Amorgos region: Insights into volcano-tectonic activity through high-resolution seismic monitoring. Seismica, 4(1). https://doi.org/10.26443/seismica.v4i1.1663", and are available at https://zenodo.org/record/15074928.

Acknowledgements. We would like to thank the scientists and personnel who participated in the installation or maintenance of the stations belonging to the HUSN and assisted with the signal processing and manual location of the recorded seismicity. The HUSN consists of the following seismic networks: HL (Institute of Geodynamics, National Observatory of Athens, doi:10.7914/SN/HL), HP (University of Patras, doi:10.7914/SN/HP), HT (Aristotle University of Thessaloniki, doi:10.7914/SN/HT), HA (National and Kapodistrian University of Athens, doi:10.7914/SN/HA), HC (Seismological Network of Crete, doi:10.7914/SN/HC), and HI (Institute of Engineering Seismology and Earthquake Engineering, doi:10.7914/SN/HI).

References

Chen, X., P. M. Shearer and R. E. Abercrombie (2012). Spatial migration of earthquakes within seismic clusters in Southern California: Evidence for fluid diffusion, J. Geophys. Res. Solid Earth, 117, B04301, doi:10.1029/2011JB008973.

Chouet, B. (2003). Volcano seismology, Pure Appl. Geophys., 160, 739-788, doi:10.1007/PL00012556.

Cocco, M. and J. R. Rice (2002). Pore pressure and poroelasticity effects in Coulomb stress analysis of earthquake interactions. J. Geophys. Res., 107, B2, 2030, doi:10.1029/2000JB000138.

Diehl, T., N. Deichmann, E. Kissling and S. Husen (2009). Automatic S-Wave Picker for Local Earthquake Tomography, Bull. Seismol. Soc. Am., 99, 3, 1906-1920, doi:10.1785/0120080019.

Druitt, T. H., R. A. Mellors, D. M. Pyle and R. S. J. Sparks (1989). Explosive volcanism on Santorini, Greece. Geol. Mag., 126, 2, 95-126, doi:10.1017/S0016756800006270.

Druitt, T. H., L. Edwards, R. M. Mellors, D. M. Pyle et al. (1999). Santorini volcano, Geological Society, London, Memoirs, 19, 176.

Evangelidis, C., N. Triantafyllis, M. Samios, K. Boukouras et al. (2021). Seismic Waveform Data from Greece and Cyprus: Integration, Archival, and Open Access, Seismol. Res. Lett., 92, 1672-1684, doi:10.1785/0220200408.

Fountoulakis, I. and C. P. Evangelidis (2025). The 2024-2025 seismic sequence in the Santorini-Amorgos region: Insights into volcano-tectonic activity through high-resolution seismic monitoring, Seismica, 4, 1, doi:10.26443/seismica.v4i1.1663.

Fytikas, M., G. Karydakis, T. Kavouridis, N. Kolios et al. (1990). Geothermal Research on Santorini. In: Hardy, D. A., Ed., Thera and the Aegean World III.2, The Thera Foundation, London, 241-249.

Ganas, A. (2025). NOAFAULTS KMZ layer Version 7.0 [Data set], Zenodo, doi:10.5281/zenodo.16728922.

Grassberger, P. and I. Procaccia (1983a). Characterization of strange attractors, Phys. Rev. Lett., 50, 5, 346-349, doi:10.1103/PhysRevLett.50.346.

Grassberger, P. and I. Procaccia (1983b). Measuring the strangeness of strange attractors. Physica D: Nonlinear Phenomena, 9, 1-2, 189-208, doi:10.1016/0167-2789(83)90298-1.

Hainzl, S., T. Kraft, J. Wassermann, H. Igel et al. (2006). Evidence for rainfall-triggered earthquake activity, Geophys. Res. Lett., 33, 19, L19303, doi:10.1029/2006GL027642.

Heiken, G. and F. McCoy (1984). Caldera Development during the Minoan Eruption, Thira, Cyclades, Greece. J. Geophys. Res., 89, 8441-8462, doi:10.1029/JB089iB10p08441.

Heiken, G. and F. McCoy (1990). Precursory Activity to the LBA Eruption, Thera, Greece, In: Hardy, D. A., Ed., Thera and the Aegean World III.2, The Thera Foundation, London, 79-88.

Kagan, Y. Y. and L. Knopoff (1980). Spatial distribution of earthquakes: The two point correlation function, Geophys. J. Int., 62, 2, 303-320, doi:10.1111/j.1365-246X.1980.tb04857.x.

Karakonstantis, A. and F. Vallianatos (2024). Santorini Volcanic Complex (SVC): How Much Has the Crustal Velocity Structure Changed since the 2011-2012 Unrest, and at What Point Are We Now? Geosciences, 14, 10, 263, doi:10.3390/geosciences14100263.

Kaviris, G., P. Papadimitriou, Ph. Kravvariti, V. Kapetanidis et al. (2015). A detailed seismic anisotropy study during the 2011-2012 unrest period in the Santorini Volcanic Complex, Phys. Earth Planet. Inter., 238, 51-88, doi:10.1016/j.pepi.2014.11.002.

Kilb, D., J. Gomberg and P. Bodin (2002). Aftershock triggering by complete Coulomb stress changes, J. Geophys. Res.: Solid Earth, 107, B4, ESE 2-1-ESE 2-14, doi:10.1029/2001JB000202.

King, G. C., R. S. Stein and J. Lin (1994). Static stress changes and the triggering of earthquakes, Bull. Seismol. Soc. Am., 84(3), 935-953, doi:10.1785/BSSA0840030935.

Kisslinger, C. and E. R. Engdahl (1973). The interpretation of the Wadati diagram with relaxed assumptions, Bull. Seismol. Soc. Am., 63, 5, 1723-1736, doi:10.1785/BSSA0630051723.

Klein, F. W. (2002). User's Guide to HYPOINVERSE-2000, a Fortran Program to Solve for Earthquake Locations and Magnitudes: U.S. Geological Survey Open-File Report 02-171, 123, https://pubs.usgs.gov/of/2002/0171/.

Lin, J. and R. S. Stein (2004). Stress triggering in thrust and subduction earthquakes and stress interaction between the southern San Andreas and nearby thrust and strike-slip faults, J. Geophys. Res.: Solid Earth, 109, B2, doi:10.1029/2003JB002607.

Makropoulos, K., G. Kaviris and V. Kouskouna (2012). An updated and extended earthquake catalogue for Greece and adjacent areas since 1900. Nat. Hazards Earth Syst. Sci., 12, 1425-1430, doi:10.5194/nhess-12-1425-2012.

Masihi, A. and T. Fischer (2025). In-Situ Vp/Vs ratio variations in seismic swarms as indicator of magmatic processes: Fagradalsfjall volcanic activity, SW Iceland. Geophys. J. Int., 241(3), 1726-1740, doi:10.1093/gji/ggaf122.

McKenzie, D. (1978). Active tectonics of the Alpine-Himalayan belt: The Aegean Sea and surrounding regions, Geophys. J. Int., 55, 1, 217-254, doi:10.1111/j.1365-246X.1978.tb04759.x.

Michas, G., V. Kapetanidis, I. Spingos, G. Kaviris et al. (2022). The 2020 Perachora peninsula earthquake sequence (East Corinth Rift, Greece): spatiotemporal evolution and implications for the triggering mechanism, Acta Geophys. 70, 2581-2601, doi:10.1007/s11600-022-00864-x.

Mrlina, J. and V. Sakkas (2026). Dynamics of Santorini Volcano During Earthquake Swarm 2025 Based on Gravity Monitoring Supported by GNSS. Pure Appl. Geophys, doi:10.1007/s00024-026-04085-x.

Nicholls, I. A. (1971). Petrology of Santorini Volcano, Cyclades, Greece. J. Petrol. 12, 1, 67-119, doi:10.1093/petrology/12.1.67.

Nomikou, P., D. Papanikolaou, M. Alexandri, D. Sakellariou et al. (2013). Submarine volcanoes along the Aegean Volcanic Arc. Tectonophysics, 597-598, 123-146, doi:10.1016/j.tecto.2012.10.001.

Papadimitriou, P., V. Kapetanidis, A. Karakonstantis, G. Kaviris et al. (2015). The Santorini Volcanic Complex: A detailed multi-parameter seismological approach with emphasis on the 2011-2012 unrest period, J. Geodyn. 85, 32-57, doi:10.1016/j.jog.2014.12.004.

Papadopoulos, G. A. (2026). A New Catalogue of Historical Eruptions in Santorini Volcano: Documentation and Completeness Analysis, GeoHazards, 7, 2, 71, doi:10.3390/geohazards7020071.

Papazachos, B. and C. Papazachou (2003). The Earthquakes of Greece, P. Ziti and Co., Thessaloniki.

Polat, G. and G. E. Altin (2026). Seismicity patterns and b-value variability in the Santorini-Amorgos system within the South Aegean volcanic arc, Acta Geophys. 74, 276, doi:10.1007/s11600-026-02007-y.

Sarlis, N. V., E. S. Skordas, E. P. Sakellis and P. A. Varotsos (2026). The 2025 South Aegean Sea Seismic Swarm Activity in Natural Time and the Generalized Gutenberg-Richter Law, Appl. Sci., 16, 6859, doi:10.3390/app16146859.

Scholz, C. H. (2019). The Mechanics of Earthquakes and Faulting. 3rd ed. Cambridge University Press, Cambridge, doi:10.1017/9781316681473.

Soubestre, J., J. Münchmeyer, Q. Higueret, N. M. Shapiro et al. (2026). Deep seismic tremors in the 2025 Santorini seismo-volcanic crisis highlight magmatic feeding from a mid-crustal reservoir, Geophys. Res. Lett., 53, e2025GL119853, doi:10.1029/2025GL119853.

Srijayanthi, G., R. S. Chatterjee, C. Kamra, M. Chauhan et al. (2022). Seismological and InSAR based investigations to characterise earthquake swarms in Jamnagar, Gujarat, India – An active intraplate region, J. Asian Earth Sci.: X, 8, 100118, doi:10.1016/j.jaesx.2022.100118.

Stein, R. S. (1999). The role of stress transfer in earthquake occurrence, Nature, 402, 6762, 605-609, doi:10.1038/45144.

Toda, S., R. S. Stein, K. Richards-Dinger and S. B. Bozkurt (2005). Forecasting the evolution of seismicity in southern California: Animations built on earthquake stress transfer, J. Geophys. Res., 110, B05S16, doi:10.1029/2004JB003415.

Toda, S., R. S. Stein, V. Sevilgen and J. Lin (2011). Coulomb 3.3: Graphic-rich deformation and stress-change software for earthquake, tectonic, and volcano research and teaching user guide. U.S. Geological Survey Open-File Report 2011-1060, doi:10.3133/ofr20111060, Available at: https://pubs.usgs.gov/of/2011/1060/.

Vallianatos, F., G. Michas, G. Papadakis and A. Tzanis (2013). Evidence of non extensivity in the seismicity observed during the 2011-2012 unrest at the Santorini volcanic complex, Greece. Nat. Hazards Earth Syst. Sci., 13, 1, 177-185, doi:10.5194/nhess-13-177-2013.

Vallianatos, F. and K. Pavlou (2021). Scaling properties of the Mw7.0 Samos (Greece), 2020 aftershock sequence, Acta Geophys., 69, 3, 1067-1084, doi:10.1007/s11600-021-00579-5.

Wadati, K. and S. Oki (1933). On the travel time of earthquake waves (Part II), J,. Meteorological Society Japan, 11, 1, 14-28, doi:10.2151/jmsj1923.11.1_14.

Wells, D. L. and K. J. Coppersmith (1994). New Empirical Relationships among Magnitude, Rupture Length, Rupture Width, Rupture Area, and Surface Displacement. Bull. Seismol. Soc. Am., 84(4), 974-1002, doi:10.1785/BSSA0840040974.

Wilding, J. D., T. A. Wang, Y. K. Liu and Z. E. Ross (2026). Cascading magmatic unrest and aseismic faulting in the Aegean Sea enabled by elastic stress relay. Sci. Adv. 12, eaec3198, doi:10.1126/sciadv.aec3198.

Yolsal-Çevikbilen, S., T. S. Irmak, C. Erman, T. Eken et al. (2026). Extensional Tectonics and Magma-Driven Seismicity Across the Santorini-Amorgos Basins, South-Central Aegean Sea: Insights from the 2025 Earthquake Swarm, Geophysical Journal International, ggag394, doi:10.1093/gji/ggag394.

Zaccagnino, D., G. Michas, L. Telesca and F. Vallianatos (2025). Precursory patterns, evolution and physical interpretation of the 2025 Santorini-Amorgos seismic sequence, Earth Planet. Sci. Lett., 671, 119656, doi:10.1016/j.epsl.2025.119656.

***CORRESPONDING AUTHOR: Kyriaki PAVLOU**,
Section of Geophysics-Geothermics, Department of Geology and Geoenvironment,
National and Kapodistrian University of Athens, 15784 Athens, Greece
e-mail: kpavlou@geol.uoa.gr

© 2026 the Author(s).
Open Access. This article is licensed under a Creative Commons Attribution 4.0 International License